Cryo-EM structure of OSCA1.2 from *Oryza sativa:* Mechanical basis of hyperosmolality-gating in plants

Koustav Maity[1*], John Heumann[2*], Aaron P. McGrath[1*], Noah J Kopcho[1], Po-Kai Hsu[3], Chang-Wook Lee[1], James H. Mapes[2], Denisse Garza[1], Srinivasan Krishnan[4], Garry P. Morgan[2], Kevin J. Hendargo[5], Thomas Klose[6], Steven D. Rees[1], Arturo Medrano-Soto[5], Milton H. Saier Jr.[5], Miguel Piñeros[4,7], Elizabeth A. Komives[8], Julian I. Schroeder[3], Geoffrey Chang[1,9†], Michael H. B. Stowell[2†]

[1]Skaggs School of Pharmacy and Pharmaceutical Sciences, University of California, San Diego, La Jolla, California, USA.

[2]Department of Molecular, Cellular and Developmental Biology, University of Colorado, Boulder, Colorado, USA.

[3]Cell and Developmental Biology Section, Division of Biological Sciences, University of California at San Diego, La Jolla, California, USA.

[4]Boyce Thompson Institute for Plant Research, Ithaca, New York, USA.

[5]Molecular Biology Section, Division of Biological Science, University of California, San Diego, La Jolla, California, USA.

[6]Department of Biological Sciences, Purdue University, West Lafayette, Indiana, USA

[7]Robert W. Holley Center for Agriculture and Health, United States Department of Agriculture–Agricultural Research Service, Cornell University, Ithaca, NY, USA.

[8]Department of Chemistry and Biochemistry, University of California, San Diego, La Jolla, California, USA.

[9]Department of Pharmacology, School of Medicine, University of California at San Diego, La Jolla, California, USA.

*These authors contributed equally.

†Co-corresponding authors

Correspondence to: GC (g1chang@ucsd,edu), MHBS (michael.stowell@colorado.edu).

Abstract

46 Sensing and responding to environmental water deficiency and osmotic stresses is
47 essential for the growth, development and survival of plants. Recently, an osmolality-
48 sensing ion channel called OSCA1 was discovered that functions in sensing
49 hyperosmolality in *Arabidopsis*. Here, we report the cryo-EM structure and function of
50 an ion channel from rice (*Oryza sativa*; OsOSCA1.2), showing how it mediates
51 hyperosmolality sensing and ion permeability. The structure reveals a dimer; the
52 molecular architecture of each subunit consists of eleven transmembrane helices and
53 a cytosolic soluble domain that has homology to RNA recognition proteins. The
54 transmembrane domain is structurally related to the TMEM16 family of calcium
55 dependent ion channels and scramblases. The cytosolic soluble domain possesses a
56 distinct structural feature in the form of extended intracellular helical arms that is
57 parallel to the plasma membrane. These helical arms are well positioned to sense
58 lateral tension on the inner leaflet of the lipid bilayer caused by changes in turgor
59 pressure. Computational dynamic analysis suggests how this domain couples to the
60 transmembrane portion of the molecule to open the channel. Hydrogen-deuterium
61 exchange mass spectrometry (HDXMS) experimentally confirms the conformational
62 dynamics of these coupled domains. The structure provides a framework to
63 understand the structural basis of hyperosmolality sensing in an important crop plant,
64 extends our knowledge of the anoctamin superfamily important for plants and fungi,
65 and provides a structural mechanism for translating membrane stress to ion transport
66 regulation.

Introduction

70 Hyperosmolarity and osmotic stress are among the first physiological responses to
71 changes in salinity and drought. Hyperosmolality triggers increases in cytosolic free
72 Ca^{2+} concentration and thereby initiates an osmotic stress-induced signal transduction
73 cascade in plants (1-3). Salinity and drought stress trigger diverse protective
74 mechanisms in plants enabling enhanced drought tolerance and reduction of water
75 loss in leaves.

77 Ion channels have long been hypothesized as sensors of osmotic stress. A candidate
78 membrane protein named OSCA was isolated in a genetic screen for mutants that
79 impair the rapid osmotic stress-induced Ca^{2+} elevation in plants (1). OSCA1 encodes
80 a multi-spanning membrane protein that functions in osmotic/mechanical stress-
81 induced activation of ion currents. However, the underlying mechanisms and whether
82 OSCA1 itself encodes an ion conducting pore specific for Ca^{2+} requires further
83 analysis. OSCA1 is a member of a larger gene family in Arabidopsis with 15 members
84 (4), and with many homologs encoded in other plants and fungal genomes.
85 Furthermore, evolutionary analyses have revealed that OSCA is distantly related to
86 the anoctamin superfamily, that includes the TMEM16 family of calcium dependent ion
87 channels (5).

Results

90 As we were interested to determine whether and how osmolality caused OSCA
91 proteins to respond to osmotic stress in crop plants, we screened five such ion
92 channels from rice, over-expressing them as TEV protease cleavable eGFP fusions
93 in *Pichia pastoris*. The *Oryza sativa* hyperosmolality-gated protein (annotated as
94 Os*OSCA1.2*, GenBank KJ920372.1) was found to have both high levels of protein
95 expression and desirable properties during purification and was therefore chosen for

96 further characterization. We purified the membrane protein to homogeneity (**Fig. S1A**)
97 and determined the oligomeric state of purified OSCA using size-exclusion
98 chromatography coupled to multi-angle laser light scattering (SEC-MALLS) analysis,
99 revealing the detergent solubilized protein to be a dimer (**Fig. S1B**).
100
101 **Functional Reconstitution of OsOscA1.2.** Reconstitution of the OsOSCA1.2
102 purified proteins into droplet interface bilayers (DIBs) indicated the purified protein is
103 fully functional, mediating ion transport (**Fig. S1C-H**). OsOSCA1.2 was active in
104 symmetrical (*cis:trans* 150:150 mM KCl) ionic conditions in the absence of any other
105 osmotically active solutes (**Fig. S1C-E**). In symmetric ionic conditions the current to
106 voltage relation for OsOSCA1.2 was quite linear, yielding a unitary conductance of
107 284± 2 pS and showing no signs of current rectification. The unitary conductance is
108 within the range of those reported recently for other OSCA proteins (e.g., between 300
109 to 350 pS in similar ionic conditions (4). Under non-symmetrical ionic conditions
110 (*cis:trans* 15:150 mM KCl), with an inwardly directed K^+ gradient, the inward single
111 channel currents reversed (E_{rev}) at about -26mV, closer to the Nernst potential for K^+
112 (E_{K+}: 54 mV after correction for ionic activities), indicating a modest selectivity for K^+
113 over Cl^- as suggested by the calculated $P_K+/P_{Cl}- = 5 \pm 1$ (**Fig. S1I**). The appearance
114 of infrequent 50% current amplitude sub-conductance state (**Fig. S1H)** was consistent
115 with the proposed assembly of two cooperative subunits as confirmed by the dimeric
116 nature of the OsOSCA1.2 channels inferred from SEC-MALLS (**Fig. S1B**). The result
117 is also consistent with and other recent studies of OSCA proteins (6, 7). Overall, the
118 above experiments confirmed functionality of our purified OsOSCA1.2 protein.
119
120 **Structure of OsOSCA1.2.** We determined a molecular structure of OsOSCA1.2 by
121 single-particle cryo-electron microscopy to an overall resolution of 4.9 Å and local
122 resolution in the membrane of 4.5 Å, revealing a dimer of C2 symmetry related
123 subunits (**Fig. S2)**. The overall dimension of the protein are 140 Å x 55 Å x 85 Å. Each
124 protomer is comprised of eleven transmembrane (TM) spanning segments, associated
125 extra- and intracellular loops and an intracellular soluble domain (**Fig. 1A**). All eleven
126 transmembrane helices and the soluble domain are well resolved in our cryo-EM maps
127 and large side chains provided suitable markers for ensuring proper sequence
128 registration during atomic model building. (**Fig. S3**). The final atomic model comprises
129 1388 out of the expected 1424 residues with good geometry and an EMringer (8) score
130 of 0.89 (**Table S1**).
131
132 According to the Transporter Classification Database (TCDB) (9), OsOSCA1.2
133 belongs to what is annotated as the Calcium-permeable Stress-gated Cation Channel
134 family (CSC; TC: 1.A.17.5) within the Anoctamin Superfamily (TC: 1.A.17). This
135 classification indicates that OsOSCA1.2 is distantly related to members of the
136 Anoctamin family (ANO; TC: 1.A.17.1) for which high-resolution 3D structure are
137 available (10, 11). Following a recently published bioinformatics approach (5), we had
138 further predicted that OsOSCA1.2 had eleven TMs and the eighth hydrophobicity peak
139 is composed of two TMs (**Fig. 1B**) based on hydropathy analysis and comparison of
140 regions with the fungal homolog *Nectria haematococca* TMEM16 (NhTMEM16) (10).
141 For convenience, we have kept the numbering convention of TMs consistent with
142 NhTMEM16, and thus we refer to OSCA1.2's additional N-terminal TM as TM0 (**Figs.**
143 **1C-D**). Despite a relatively low degree of sequence similarity, we later confirmed that
144 OsOSCA1.2 shares significant structural homology to the TMEM proteins with respect

145 to ten of the eleven transmembrane regions, corresponding to TMs1-10 in the mouse
146 TMEM16A (mTMEM16A) structures.

147

148 TM0 threads from the extracellular N-terminal end of the protein through the
149 membrane, linking to TM1 via a ~50 residue strand that is likely conformationally
150 flexible. This portion of the protein is the only region not fully resolved in our density
151 maps (**Figs. 1B-D**). A short helix on the cytoplasmic side then precedes TM1 and the
152 C-terminal end of TM2 leads into the soluble cytosolic region of ~170 residues. The
153 remaining helices represent the anoctamin domain, encapsulating the pore region for
154 ion conductance. TMs3-4 are located on the outer edge of the transmembrane region
155 and are tilted with respect to the membrane. TMs7-8 are shorter in length and are the
156 only TMs that do not span the entire length of the membrane, with the connecting loop
157 (residues 578-583) being embedded in the membrane and consisting of hydrophobic
158 residues.

159

160 The soluble domain is located on the intracellular side of the channel joining TM2
161 and TM3 and makes important structural contacts with the C-terminus (**Figs. 1B-D**).
162 A core globular domain comprises a four-stranded β-sheet buttressed by two short
163 helices that interestingly forms a canonical RNA recognition motif (RRM) fold (12).
164 Unlike true RNA binding RRM proteins, OsOSCA1.2 includes a fusion of a distinct 70-
165 residue appendage between β-strands 2 and 3. These long, extended helical arms
166 protrude out from the RRM domain and are located proximal to and in the plane of
167 what would be the inner-leaflet side of the plasma membrane.

168

169 The dimer interface represents only a small percentage (~2.7%) of the surface area
170 of each protomer, burying only ~1116 Å^2 surface area comprised by interactions
171 formed between the soluble domains (**Figs. 2A-B**) (13). Interface residues Q334,
172 T335, Q336, Q337, T338, S339, L681, Q682, and E683 from both subunits likely make
173 several hydrogen bonds and hydrophobic interactions (**Fig. 2C**). Interestingly, the TMs
174 from each subunit do not cause significant interactions contributing to the dimer
175 interface. The orientation and offset of the two halves of the dimer creates a large
176 cavity between the two protomers, which, as predicted in other AtOSCA structures (6,
177 7, 14), is likely filled with lipids when embedded in the cell membrane.

178

179 The ion conductance pore of OsOSCA1.2 is contained within each monomeric
180 subunit (**Fig. 2D**), and formed between TMs 3-7 as suggested by the topological
181 similarities with mTMEM16A. Using the program HOLE to visualize the putative ion
182 permeation pathway (15), the overall shape of the pore resembles an hourglass. The
183 extracellular and an intracellular vestibule are bridged by a narrow neck region that is
184 about 20 Å long through the membrane. The putative pore has an opening more than
185 12Å wide towards the extracellular side and narrows into the 'neck' region
186 approximately 15 Å down the conduction pathway. The tightest juncture is ~0.8 Å wide,
187 suggesting that this channel structure is in a closed conformation. The calculated pore
188 profile predicts that the hydrophobic residues F511, F512, and Y515 on TM6 and V472
189 and Y464 on TM5 forms a gate that completely blocks the channel pore (**Fig. 2E**).

190

191 **OsOSCA1.2 computational dynamics.** The DynOmics suite allows prediction and
192 identification of candidate functional sites, signal transduction, and potentially
193 allosteric communication mechanisms, leveraging rapidly growing structural
194 proteomics data (16). The suite integrates two widely used elastic network models

195 while taking account of the molecular environment like the lipid bilayer providing
196 collective dynamics of structural resolved systems. We used DynOmics to do
197 molecular dynamic simulations on our OsOSCA1.2 dimer model after embedding in
198 the membrane, looking for regions that could potentially serve as functionally
199 important sensors, broadcasters, and receivers (**Fig. 3A**). Our results revealed that
200 the extended intracellular helical arms could communicate conformational
201 perturbations, having the propensity to act as a broadcaster/receiver, extending to the
202 central core sheet structure of the soluble domain and, more interestingly, TM6, which
203 is proposed to be the ion gating helix in related structures (6, 7, 10, 11, 14).
204
205 **OsOSCA1.2 experimental dynamics.** In order to further understand and probe local
206 conformational dynamics of OsOSCA1.2, we used HDXMS. This approach utilizes the
207 exchange that occurs between protons linked to amide bonds and protons or
208 deuterium nuclei from solvent molecules to provide experimental information
209 regarding regional solvent accessibility and dynamics. When a protein is added to a
210 solution containing excess D_2O, hydrogen-deuterium exchange occurs most rapidly
211 for protons which are exposed to solvent and unconstrained by intermolecular
212 hydrogen bonds. Protease digestion and chromatographic separation facilitate the
213 quantification of deuterium nuclei incorporated throughout the protein as measured by
214 mass spectrometry (17). For the hydrogen-deuterium exchange to occur in well-folded
215 regions, a protein must sample exchange-competent conformations which expose
216 amide protons. Thus, the uptake of deuterium over time reflects the local dynamics
217 that individual regions of a protein undergo in solution (18).
218
219   HDXMS measurements using detergent solubilized OsOSCA1.2 protein resulted
220 in the identification of 32 peptides, which constitute 34.5% coverage of the molecule
221 (**Figs. 3B and S4A**), including the helical arms that were predicted to dynamically
222 couple to the presumed gating helix TM6 and most likely to be responsible for sensing
223 lateral tension in the membrane. The helix closest to the inner leaflet side of the
224 membrane was covered by two peptides (corresponding to residues 244-257 and 245-
225 257). Deuterium incorporation profiles revealed that this region was tightly protected
226 from exchange, indicative of rigid dynamics or association with a nearby surface (**Fig.
227 3C**). The following segment was also covered by two peptides (residues 258-279 and
228 258-286), which correspond to the C-terminal end of the protected helix and a nearby
229 loop in our structure. This region was ~25% saturated with deuterium nuclei at the
230 earliest measured time point of 1 minute, indicating rapid exchange associated with
231 conformational flexibility. The remainder of this segment increased deuterium content
232 by ~5% over 5 minutes suggesting conformational motions that gradually increased
233 exposure to solvent. The helix farther from the membrane was covered by three
234 peptides (residues 287-320, 289-320, 305-320) and similarly displayed rapidly-
235 exchanging amides and ongoing deuterium exchange. Mass spectra from peptides
236 corresponding to the unstructured loop and helix farther from the membrane all
237 displayed bimodal deuterium uptake, which was more prominent among peptides
238 corresponding to the loop (**Fig. S4B**). The ongoing dynamics in sharp contrast to the
239 rigidity of the helix (residues 241-266) closer to the membrane. Despite being spatially
240 and sequentially near each other, these two intracellular helices have very different
241 dynamic properties.
242
243 **Topological insertion of OSCA in tA201 Cells.** As the OSCA family inserts an
244 addition helix, TM0, we investigated the orientation of the ion channel in the cell

5

245 membrane in mammalian human embryonic kidney tsA201 cells. The topological
246 prediction and structures suggested that the N- and C-termini of the molecule were on
247 opposite sides of the membrane (**Fig. 1B)**. We, therefore, made two C-terminal HA-
248 tagged (YPYDVPDYA) cDNA constructs of OsOSCA1.2 and AtOSCA1 in a pcDNA3.1
249 vector. Human kidney cell-line tsA201 cells were transfected with both of these
250 constructs (**Figs. S5A-B**) and, after 48 hours, the cells were stained with anti-HA
251 antibody conjugated to Alexa488 without permeabilization (see Methods). Our results
252 suggest that the C-terminus of the molecule was accessible only from outside the cell.
253
254 **Osmotic stress response of OsOSCA1.2.** It was suggested that the orthologs of
255 OsOSCA1.2 in *Arabidopsis*, AtOSCA1 and AtOSCA1.2, are osmotic stress responsive
256 cation channels (1, 19). We, therefore, explored whether changes in the intracellular
257 free Ca^{2+} concentration occur in response to osmolality changes in tA201 cells using
258 a ratiometric fluorescent indicator, Fura-2AM (**Fig. S6**). No obvious differences were
259 observed between control and OsOSCA1.2-expressing tA201 cells in hypoosmotic
260 (168 mosmol kg^{-1}) and hyperosmotic (627 mosmol kg^{-1}) calcium responses (**Figs.
261 S6A-B**, n > 23 OsOSCA1.2-expressing cells). Rapidly induced fluorescence ratio
262 changes were observed in response to exogenous ATP in the same OsOSCA1.2-
263 expressing tA201 cells as controls (**Fig. S6A**), suggesting that Fura-2 can efficiently
264 report intracellular calcium changes in these experiments.
265
266 **Discussion**
267 OsOSCA1.2 shares overall protein fold and topology with other recently determined
268 homologous structures from *A. thaliana* (6, 7, 14). A superposition of these structures
269 with OsOSCA1.2 showed a significant difference (rmsd ~3-4Å) for the pore-lining
270 helices (TM3-7) along with TM0 and TM8 (**Fig. 4A**). When comparing intracellular
271 soluble domains, the extended helical arms of OsOSCA1.2 had noticeable differences
272 compared to that of AtOSCA1 (**Fig. 4A)**. These differences are likely due to a
273 combination of conformational flexibility inherent in the detergent solubilized protein
274 and structural difference between species.
275
276 OsOSCA1.2 also shares structural homology to the TMEM family (mTMEM16A,
277 NhTMEM16) when comparing monomeric transmembrane domain regions. However,
278 they differ significantly in the regions of extra- and intra-cellular loops and domains as
279 well as the intermolecular packing arrangement of the respective dimers. The dimer
280 interface of mTMEM16A buries less surface area (~2%) compared to OsOSCA1.2 and
281 most of the interactions are mediated through the TM domains. The intracellular
282 domains of mTMEM16A and nhTMEM16, which are formed by the N and C-termini of
283 the molecule, do not contribute to the formation of the dimer (**Fig. 4B**). In contrast,
284 OsOSCA1.2 dimerizes mostly through interactions formed between the opposing
285 intracellular soluble domains. This distinct dimeric packing resulted in a more
286 pronounced offset between protomers, that is ~20 Å wider for OsOSCA1.2 compared
287 to NhTMEM16 or mTMEM16A. In our OsOSCA1.2 structure, the extended helical arm
288 in the intracellular soluble domain make hydrophobic contacts with the loop connecting
289 the gating helix TM6 (**Fig. 4C**), suggesting a possible role for the helical 'arms' in
290 sensing the membrane tension and, in turn, transmitting these
291 conformational/mechanical changes to gate ion conductance (**Fig. 4D**). This feature
292 is, of course, missing in TMEM16 channels as Ca^{2+} ions control gating.
293

6

Our OsOSCA1.2 structure likely represents the non-conducting state conformation as no tension, pressure or osmolality mismatch was applied between the intracellular and extracellular sides of the OsOSCA1.2 protein during cryo-EM sample preparation. Indeed, the tightest juncture in the pore is ~0.8 Å wide (**Fig. 2D-E**). Our DIBs study suggests that the reconstituted OsOSCA1.2 protein could conduct ions (**Fig. S1E**). Interestingly, when the OsOSCA1.2 structure was compared to mTMEM16A, we found a π-helical turn at TM6 near the 'neck' region of the pore that might be associated with ion gating and channel opening in a similar fashion (Ca^{2+} activated π-to-α transition) to that observed in mTMEM16A (11, 20). The regulatory Ca^{2+} binding site composed of acidic and polar residues (E702 and E705 from TM7, E734, and D738 from TM8, and N651 and E654 from TM6 in mTMEM16A) are well conserved in the TMEM16 family (**Fig. 4E**). However, when compared to the corresponding same region in OsOSCA1.2, the negatively charged residues D519 and E527 on TM6 and polar residue R568 on TM7 locate spatially different (**Fig. 4F**). Therefore, OsOSCA1.2 will likely not specifically bind calcium ions in this region.

Computational dynamic studies using our OsOSCA1.2 model and experiments using hydrogen-deuterium exchange with detergent solubilized OsOSCA1.2 protein provided a molecular structural basis of how OsOSCA1.2 couples osmotic stress to induce ion channel gating in the membrane spanning region. Taken together, both studies predict and suggest that the extended helical arms (residues 241-266) have the mechanical rigidity and propensity to act as a broadcaster/receiver, transmitting conformational changes caused by lateral tension in the membrane to TM6 (**Figs. 3, 4F**), which is important for gating ion conductance. In addition, information from HDXMS revealed the presence of bimodal deuterium exchange throughout the OsOSCA1.2 (**Figs 3B-C and S4B**), most prominently within the helical arms (residues 258-320) and some extracellular loops (residues 489-511). Bimodal exchange is indicative of multiple correlated unfolding processes occurring in the observed regions (21). Interestingly, in each peptide where bimodal peaks were observed, the two peaks remained equal in intensity over the entire course of the experiment, suggesting at least two distinct conformational states occupied by the molecular ensemble at equilibrium in the resting state.

Several electrophysiological studies have used mammalian cells over-expressing OSCA channels to measure conductance gated by direct mechano-transduction or pressure (1, 4, 6). Interestingly, we found that the C-terminus and presumably the entire cytosolic domain (residues 191-363) were on the outside when OSCA channels were over-expressed in mammalian cells (**Fig. S5**). This finding suggests and could explain why channel opening due to changes in ion concentration may be impaired. As previous studies suggested Ca^{2+} conductance, we further probed ion flux using FURA2 using these cells as proxy for calcium but found no changes relative to controls for either hyper- or hypo-osmotic conditions (**Fig. S6**). It remains unclear whether or not these ion channels can be gated by changes in ion concentration. Interestingly, analysis of the taxonomic distribution of different OSCA fragments suggests that TM0 is restricted to plants and that the cytosolic domain (residues 191-363; cytoL2) is probably distributed similarly to the rest of OSCA family (**Fig. S7-9 and Table S1**). In fungi and plants, the N-terminus of TM0 is predicted to be on the outside with the osmo-sensing cytosolic domain inside the cell (**Fig. 1B**). OSCA may be inserted in the membrane differently between mammalian and plant/fungi cells and may be an important consideration in their functional study.

344
345   Several important questions remain regarding these OSCA channels and their role
346   in crops. For example, the specificity of endogenous ions conducted by OsOSCA1.2
347   or by other members within their greater family is still unknown. It will certainly be a
348   challenge to assign function to all of these proteins individually as these channels are
349   members of large gene families. Although we present a structure of OsOSCA1.2 along
350   with computational and experimental dynamics, the detailed function mechanism(s)
351   coupling lateral tension in the membrane by OsOSCA1.2 to channel gating remains to
352   be addressed in future studies. These studies will certainly be challenging given the
353   transient nature of channel gating.
354
359

Methods

Expression and Purification of OsOSCA1.2. We cloned OsOSCA1.2 (GenBank KJ920372.1) and made TEV protease cleavable green fluorescent protein (GFP) fusions into the pPICZc vector, and tested expression in *Pichia pastoris*. Expression vectors were linearized using *Pme*I and electroporated into competent *P. pastoris* KM71H cells (Life Technology). The resulting transformants were cultured and induced in small scale to screen for target expression based on the intrinsic GFP fluorescence of cells and also from an anti-His western blot of whole cell lysate. OsOSCA1.2 was found to show both high levels of expression, and desirable properties during purification (described below) and was therefore chosen for further characterisation. Yeast clones selected for their high expression of OsOSCA1.2 were grown in minimal glycerol (4%) media, supplemented with 0.4% phosphoric acid and 0.024% trace metals at 28°C in a New Brunswick BioFlo 415 (Eppendorf). The pH of the media was titrated to pH 5 prior to inoculation and adjusted during the vegetative growth phase using 50% ammonium hydroxide. The dissolved oxygen (DO) was maintained at 10% minimally through-cascaded agitation until a DO spike occurred. The fermentation culture was then induced at pH 5 by slow methanol addition for 16-18 hours.

Cells were harvested and resuspended in cold lysis buffer (20 mM Tris-HCl pH 8.0, 100 mM NaCl, 15% glycerol, 23.4 mM leupeptin, 7 mM E-64, 4 mM chymostatin, 14.5 mM pepstatin A, 1 mM PMSF, 25 mM benzamidine), and they were lysed by a single passage through a cell disruptor (TS-Series, Constant Systems, Inc.) at 40,000 psi. Cellular debris were removed by centrifugation (12,500 x g, 20 minutes, 4°C) and the supernatant continued onto a 38,400 x *g* spin for 4 hrs to fractionate the plasma membrane. The membrane fraction was resuspended in lysis buffer and frozen at -80°C.

Membranes were solubilized with 1% n-dodecyl-β-D-maltopyranoside (DDM) and 0.1% sodium cholate for ~90 min at 4°C. Insoluble material was removed by centrifugation (38,400 x *g*, 4 °C for 60 minutes) and 15 mM imidazole was added to the supernatant before batch binding to Ni-NTA agarose resin (Qiagen). The bounded resin was sequentially applied to a gravity column housing and washed with buffer A (20 mM HEPES pH 8.0, 150 mM NaCl, and 0.03% DDM, 0.003% cholesteryl hemisuccinate) and an imidazole gradient was applied. Bound target protein was eluted with buffer A containing 300 mM imidazole, concentrated to ~8 mL, desalted (HiPrep 26/10, GE Healthcare) and subjected to TEV protease digestion for 12 hours at 4°C. TEV digested sample was reapplied to Ni agarose (Qiagen) to rebind the TEV protease and the C-terminal His-GFP tag. The collected OsOSCA1.2 was then concentrated to ~1 mL and ultraspun at 95,000 rpm (TLA120.1 rotor) for 15 minutes at 4°C. The sample was then applied to a Superdex 200 increase size-exclusion column (GE Healthcare) pre-equilibrated with 20 mM HEPES pH 8.0, 150 mM NaCl, 0.06% *n*-undecyl-β-D-maltopyranoside 0.2 mM tris(2-carboxyethyl)phosphine, and 0.01% cholesteryl hemisuccinate, and run at 4°C. Peak fractions off the size-exclusion chromatography column were checked using sodium dodecyl sulfate polyacrylamide gel electrophoresis (SDS-PAGE) and directly snap frozen at a concentration of ~3 mg/mL.

9

Determination of the molecular mass of OsOSCA1.2 using SEC-MALLS. Size-exclusion chromatography coupled to multi-angle laser light scattering (SEC-MALLS) was performed using a Superdex 200 Increase 10/300 GL size exclusion column (GE Life Sciences) connected in series to a miniDAWN TREOS light scattering detector and an Optilab T-rEX refractive index detector (Wyatt Technology, Santa Barbara, CA, USA). Purified OsOSCA1.2 was injected onto the column with 20 mM HEPES pH 8.0, 150 mM NaCl, 0.03% *n*-dodecyl-β-D-maltopyranoside, 0.2 mM TCEP, 0.001% sodium cholate and 0.02% cholesteryl hemisuccinate and run at 0.4 mL/min. The elution was monitored in-line with three detectors, and the molecular weights of the protein-micelle complex, the micelle and the protein were calculated using ASTRA v.6 software (Wyatt Technology) in conjugate mode as previously described (22).

Functional reconstitution of OsOSCA 1.2 into droplet interface bilayers (DIBs). Lipids of *E. Coli* extract polar (Avanti #100600) were dried under nitrogen and vacuum desiccated for one hour, before resuspending in reconstitution buffer (10 mM HEPES, pH 7.4, 150 mM KCl) to a final concentration of 10 mg/ml. The resuspended lipids were incubated for a minimum of 20 min followed by addition of 0.1% DM. The mixture was allowed to sit at room temperature for 30 min followed by bath sonication for 5 cycles of 1 minute sonication and 2 min on ice. Purified OsOSCA1.2 was then mixed at a protein-lipid ratio of 1:500 (w/w) with the detergent saturated liposomes. The protein was reconstituted by removal of detergents by the detergent-dilution method (23). OsOSCA1.2 containing proteoliposomes were resuspended to a final lipid concentration of ~5mg/ml, extruded through a 100 nm filter, and stored at -80°C until use. Ion channel reconstitution into droplet interface bilayers (DIBs) was done as detailed elsewhere (24-26). Briefly, a lipid asymmetric droplet-droplet (~200 nl) configuration (27) was obtained by placing OsOSCA1.2 containing proteoliposomes in *E. coli* extract polar lipids on the agar coated head-stage Ag electrode and POPC: POPS: DOPA (1:1:0.5; Avanti #850457, #840034, #840875) liposomes on the reference electrode. The droplets were incubated in a hexadecane (Sigma # H6703) medium for 5-10 min to allow formation of monolayers on each droplet. The two droplets were then brought into contact with each other and the formation of bilayers was monitored using a triangular wave protocol. Incorporation of ion channels into the bilayer were detected as discrete fluctuations in current amplitude under voltage clamp conditions. Data were acquired using a Dagan 3900A amplifier and pCLAMP 10 software (Molecular Devices, Sunnyvale, CA). Data were filtered at 1 kHz and sampled at 250 kHz and using a Digidata 1440A. Downward deflections traces represent inward currents (*cis* to *trans*), whilst upward deflections represent outward currents (*trans* to *cis*). Single channel data analysis was performed using Clampfit 10 (Molecular Devices). The cation ionic concentrations of all solutions were verified experimentally via conductively coupled plasma emission spectrometry and their ionic activities were calculated using GEOCHEM-EZ (28). All experiments were performed at room temperature.

EM Data Collection. Quantifoil 1.2/1.3 Au(Quantifoil Micro Tools GmbH, Germany) or C-Flat 1.2/1.3 300 (Protochips, Raleigh, NC) mesh grids were glow discharged for 30 seconds at 110mA (Emitech). Four microliters of OSCA1.2 at a concentration of 1.8 mgs/ml was applied to the grids, blotted for 2.5s at a relative humidity of 100% and plunge frozen in liquid ethane using a FEI Vitrobot Mark 2 (FEI Company, Hillsboro, OR). Two image sets were collected. The first data set was collected using defocus phase contrast on an FEI Tecnai F30 microscope(FEI Company, Hillsboro, OR)

10

operating at 300kV with a K2 Summit camera(Gatan, Inc., Pleasanton, CA) at a nominal magnification 31,000x in super resolution mode with a pixel size of 0.636Å using SerialEM software(Mastronarde Group, Boulder, CO). A total of 40 frames at 200 ms per frame were recorded for each image at a camera dose rate of 8 electrons/pixel/s. A total of 342,910 particles covering a defocus range from -0.8 to -2.8 microns were used to determine an initial 6.0 Å resolution map that was utilized to build a poly alanine model (**Table 1**). A higher resolution data set was collected using a FEI Titan Krios equipped with a Volta Phase Plate, GatanEnergy Filter and a K2 summit camera (Gatan, Inc., Pleasanton, CA). Data were collected at a nominal magnification of 105,000x in super resolution mode and a total of 64,096 individual particle images at a fixed target defocus of -0.5 micron defocus were used to determine the structure at 4.9 Å resolution (**Table 1 and Fig. S2**).

EM Data Processing. The Tecnai F30 data set consisted of a total of 9,691 micrographs in 3 groups were selected for initial processing after motion correction using MotionCor2 and CTF estimation with Gctf. Non dose-weighted micrographs were used for CTF estimation, and dose-weighted micrographs for all other processing. Approximately 1,000 manually picked particles from each group were used to generate 2X binned templates (2.542 Å pixel size) which were used for autopicking in Relion. Micrographs. Autopicked particles were manually screened, and 499,167 particles extracted for further processing in cryoSPARC. 2D classification and selection yielded 342,910 particles which were then used for initial model construction and auto-refinement. Auto-refinement and masking with C2 symmetry yielded a map with 6.0 Å resolution by GSFSC corrected for the effects of masking. Local resolution estimation in cryoSPARC indicated that the core regions have resolutions ranging from 4.5 Å to 6.0 Å.

The Titan Krios data set consisted of a total of 2,408 micrographs that were motion corrected using MotionCor2 and CTF's estimated using Gctf. Results were imported into Relion 2.1, A total of 1,126 corrected micrographs were selected for further processing after screening for excessive motion, and poor or poorly estimated CTF's. 1,134 particles were manually picked, classified in 2D, and the selected templates used to auto-pick 372,278 particles. Further screening resulted in selection of 650 micrographs containing 169,655 particles for additional processing. 2X binned (2.76 Å pixel size) particles were extracted and processed through 2 rounds of 2D classification and selection, resulting in 64,096 remaining particles. 3D auto-refinement with C2 symmetry using these particles and an initial model from the previous defocus contrast refinement yielded a model with 7.4 Å resolution. Re-extraction with unbinned pixels and subsequent refinement led to no improvement in resolution at this stage. 3D classification into 10 classes and subset selection yielded 5 subsets (best single class, best 2 classes, best 5 classes, and all classes) which were used for another round of re-extraction and auto-refinement. The best resolution resulted from using all 64,096 particles and was unchanged at 7.4 Å. Masking and post-processing resulted in an estimated resolution of 6 A. At this point, the 64,096 extracted particles were transferred to cryoSPARC, and subsequent processing performed in cryoSPARC. 3D auto-refinement with C2 symmetry using all 64,096 particles and an initial model constructed using a subset of 16,438 selected particles resulted in an GSFSC estimated resolution of 4.9 Å. The auto-refined, unsharpened map was further sharpened with a B-factors ranging from -350 to -600 out to a cutoff

11

508 of 3.5 Å for modelling and a map with a B-factor of -530 was used for subsequent
509 model building and refinement.
510
511 **Model building and Refinement.** An initial polyalanine model was built using the 6.0
512 Å resolution map with multiple rounds of real space refinement in Phenix/COOT (29,
513 30). In order to determine the absolute hand at this resolution, the initial and inverted
514 model were used for molecular replacement using X-ray diffraction data set that
515 extended to 9 Å in resolution. Only one model provided a solution to the MR search.
516 Subsequent use of this initial model and the observation of the helical hand in the 4.9
517 Å resolution map further confirmed the correctness of the assigned hand. The full
518 atomic model was built into the higher resolution map using multiple rounds of building
519 and real-space refinement in COOT and Phenix. The density maps within the
520 transmembrane region were of sufficient quality to readily identify large aromatic side
521 chains (**Fig. S3**) and helped to confirm the correct sequence registration. Comparison
522 to the recently determined structures of the AtOSCA1.2 (6, 14) further confirmed the
523 correctness of our model despite the lower calculated overall resolution of our map.
524
525 **Image Processing.** Motion-corrected projections with pixel size 1.271 Å (F30) and
526 1.384 Å (Titan Krios), with and without dose-weighting, were constructed using
527 MotionCor2 (31) with 2X binning and grouping. The CTF estimation was performed
528 using Gctf (32) followed by manual selection to remove micrographs with poor or
529 incorrectly fit CTF, poor astigmatism and contamination. Manual and semi-automated
530 particle picking was done using RELION 2.1 (33), followed by sorting and another
531 round of manual over-reading to remove low quality micrographs. Subsequent
532 refinements were carried out in RELION or cryoSPARC (34). Local resolution
533 estimation was performed using cryoSPARC or ResMap (35).
534
535 **Hydrogen-deuterium exchange mass spectrometry (HDXMS).** HDXMS
536 measurements were made using a Synapt G2Si system (Waters Corporation).
537 Deuterium exchange reactions were carried out by a Leap HDX PAL autosampler
538 (Leap Technologies, Carrboro, NC). Deuterated buffer was prepared by lyophilizing
539 10 mL of 20 mM HEPES, pH 8.0, and 150 mM NaCl. Lyophilized buffer was
540 resuspended in 10 mL of 99.96% D_2O immediately before use, to which was added
541 powdered *n*-undecyl-β-D-maltopyranoside to a final concentration of 0.06% and
542 cholesterol hemisuccinate to a final concentration of 0.01%. Each deuterium exchange
543 time point (0 min, 1 min, 2.5 min, 5 min) was measured in triplicate. For each
544 measurement, 4 µL of protein at a concentration of 5 µM was mixed with 36 µL of D_2O
545 buffer at 25 °C. Deuterium exchange was quenched by combining 35 µL of the
546 deuterated sample with 65 µL of 0.1% formic acid and 3M guanidinum-HCl for 1 min
547 at 1 °C. The quenched sample was then injected in a 50 µL sample loop and digested
548 by an inline pepsin column (Pierce, Inc.) at 15 °C. The resulting peptides were
549 captured on a BEH C4 Vanguard precolumn at a flow rate of 400 µL/sec, separated
550 by analytical chromatography (Acquity UPLC BEH C4, 1.7 µM, 1.0 × 50 mm, Waters
551 Corporation) using 7−85% acetonitrile in 0.1% formic acid over 7.5 min, and analyzed
552 in a Waters Synapt G2Si quadrupole time-of-flight mass spectrometer following
553 electrospray injection.
554
555 Data were collected in Mobility, ESI+ mode, mass acquisition range of 200−2000
556 (m/z), scan time 0.4 s. Continuous lock mass correction was performed using infusion
557 of leu-enkephalin (m/z = 556.277) every 30 seconds (mass accuracy of 1 ppm for

558 calibration standard). For peptide identification, data were collected in MS^E (mobility
559 ESI+) mode. Peptide masses were identified following triplicate analysis of 10 µM
560 OsOSCA1.2, and the data were analyzed using PLGS 2.5 (Waters Corporation).
561 Peptide masses were identified using a minimal number of 250 ion counts for low
562 energy peptides and 50 ion counts for their fragment ions. The following parameters
563 were used to filter peptide sequence matches: minimum products per amino acid of
564 0.2, minimum score of 7, maximum MH+ error of 5 ppm, and a retention time RSD of
565 5%, and the peptides had to be present in two of the three ID runs collected. After
566 identification in PLGS, peptides were analyzed in DynamX 3.0 (Waters Corporation).
567 Deuterium uptake for each peptide was calculated by comparing the centroids of the
568 mass envelopes of the deuterated samples with the undeuterated controls. To account
569 for back-exchange and systematic autosampler sample handling differences, the
570 uptake values measured at the 1 min time point were divided by 0.79. The longer 2.5
571 min and 5 min deuteration time point deuteration values were divided by 0.75. Data
572 were plotted as number of deuterons incorporated vs time. The Y-axis limit for each
573 plot reflects the total number of amides within the peptide that can possibly exchange.
574 Each plot includes the peptide MH+ value, sequence, and sequential residue
575 numbering.

577 **Production of OsOSCA1.2/AtOSCA1 stable expression cell-line.** An epitope HA
578 tag (YPYDVPDYA) was introduced onto the 5′ end (HA-OsOSCA1.2) or the 3' end
579 (OsOSCA1.2-HA, AtOSCA1-HA) of the full-length OsOSCA1.2 or AtOSCA1 cDNAs
580 by PCR. The cDNA was amplified using the *PfuUltra II* Fusion HS DNA Polymerase
581 (Agilent Technologies, Inc., Santa Clara, CA). PCR products were then subcloned into
582 the pcDNA3.1 vector (Thermo Fisher Scientific, Waltham, MA). The cDNA inserts were
583 verified by sequencing (GENEWIZ, South Plainfield, NJ). After linearization of the
584 vectors with *Pvu I* enzyme, the vectors were transfected to tsA201 cells (ECACC)
585 using Lipofectamine LTX with Plus Reagent (Thermo Fisher Scientific, Waltham, MA).
586 Stable cell-lines were selected 48 h post-transfection with 1mg/ml of Geneticin
587 (Thermo Fisher Scientific, Waltham, MA).

589 **Immunofluorescence assay.** OsOSCA1.2/AtOSCA1 expressing cells were plated on
590 poly-L-lysine-coated glass coverslips in 24-well plates. After 48 hours, cells were fixed
591 with 4% paraformaldehyde/PBS. And then cells were blocked with 3% BSA/PBS for
592 30 min. Expression of OsOSCA1.2/AtSCA1 were detected with Alexa Fluor 488 anti-
593 HA (16B12) antibody (BioLegend, San Diego, CA) in PBS, 1% BSA/PBS for 1 h.
594 Samples were visualized on a fluorescence microscope (EVOS Cell Imaging Systems,
595 Thermo Fisher Scientific).

597 **[Ca^{2+}]$_i$ Imaging in tA201Cells.** Intracellular Ca^{2+} concentration changes in tA201 cells
598 in were observed using the ratiometric Ca^{2+} indicator dye, Fura-2 (36). The
599 mammalian cells were transfected with the *pCDNA3.1* (control) or the *pCDNA3.1-*
600 *OsOSCA1.2-HA* vector were cultured on poly-L-lysine coated glass bottom 35 mm
601 dish for 16 to 24 hrs. Cells were loaded with 5 µM Fura-2AM (F1221, Invitrogen,
602 Eugene, OR) in loading buffer (~286 mosmol kg^{-1}; 130 mM NaCl, 3 mM KCl, 0.6 mM
603 MgCl$_2$, 0.1 mM CaCl$_2$, 10 mM glucose, 10 mM HEPES, adjusted to pH 7.4 with NaOH)
604 and kept in the dark for 45 min, washed twice by assay buffer (~286 mosmol kg^{-1}; 130
605 mM NaCl, 3 mM KCl, 0.6 mM MgCl$_2$, 2 mM CaCl$_2$, 10 mM glucose, 10 mM HEPES,
606 and adjusted pH to 7.4 by NaOH) for 5 min each time, and then incubated with 1 mL
607 assay buffer for Ca^{2+} imaging. For hypoosmotic treatments, 1 mL hypertonic buffer (3

13

608   mM KCl, 0.6 mM MgCl$_2$, 2 mM CaCl$_2$, 10 mM glucose, 10 mM HEPES, and adjusted
609   to pH 7.4 using NaOH) was added into the original 1 mL assay buffer resulting in a
610   final osmolality ~168 mosmol kg^{-1} of the incubation buffer. For ATP treatments, 20 μl
611   of 1 mM ATP was added into the 2 mL ~168 mosmol kg^{-1} incubation buffer resulting a
612   final ATP concentration of 10 μM. For hyperosmotic treatments, 1 mL of hypertonic
613   buffer (650 mM sorbitol, 130 mM NaCl, 3 mM KCl, 0.6 mM MgCl$_2$, 2 mM CaCl$_2$, 10
614   mM glucose, 10 mM HEPES, and adjusted to pH 7.4 with NaOH) was added resulting
615   in a final osmolarity ~627 mosmol kg^{-1} in the incubation buffer. The osmotic
616   concentrations of the buffers were determined by using a Wescor 5500 Vapor
617   Pressure Osmometer. Time-resolved Fura-2 imaging was performed using an Eclipse
618   TE300 inverted microscope equipped with a Plan Fluor 40x/1.30 Oil objective DIC H
619   ∞/0.17 WD 0.2 (Nikon, Tokyo, Japan), a ET-Fura2 filter set 79001 (EX340x, EX380x,
620   ET510/80m; Chroma, Bellows Falls, VT), a Mac 2002 System automatic controller, a
621   Cool SNAP HQ camera (Photometrics, Tucson, AZ), and guided by the MetaFluor
622   software version 7.0r3 (Molecular Devices, Sunnyvale, CA). Fluorescence images
623   excited at 340 nm or 380 nm were collected at 200 ms exposure every 5 seconds.
624   Emission ratios for 340/380 nm excitations in cells were processed and analyzed using
625   Fiji (37).
626
627   **Data availability**
628   Cryo-EM maps of OsOSCA1.2 has been deposited to the Electron Microscopy Data
629   Bank under accession codes XXXX and XXXX. Atomic coordinates of OsOSCA1.2
630   have been deposited in the PDB under ID XXXX. All other data are available upon
631   request to the corresponding author(s).

14

632

Table 1. Cryo-EM data collection, 3D reconstruction and model building		
Data Collection and Processing		
Microscope	FEI Tecnai F30	FEI Titan Krios
Voltage (kV)	300	300
Camera (mode)	Gatan K2 Summit (40 frame super-res movies)	Gatan K2 Summit (40 frame super-res movies)
Target Defocus (μm)	-0.8 to -2.8	-0.5 Volta Phase Plate
Pixel size (Å)	0.6355	0.6920
Imposed symmetry	C2	C2
Electron dose (e-/ Å^2)	45.5	40.8
Initial particle images	499,157	169,655
Final particle images	342,910	64,096
Map resolution (Å) FSC 0.143 Max local resolution (Å)	6.0 Å 4.8 Å	4.9 Å 4.5 Å
Model Building and Refinement		
Map sharpening B factor (Å^2)	-800	-530
Protein residues (expected)	1388 (1424)*	1388 (1424)
R.M.S. Z score Bond Lengths (# Z>2) Bond Angles (# Z>2)		0.30 (2) 0.44 (6)
Validation MolProbity score Clashscore EMRinger score Poor rotamers (%)		1.98 7.99 0.89 0.00
Ramachandran plot Favored (%) Outliers (%)		90.1 0.0

633

Figure 1

A.

1

2

3

4

B.

C.

D.
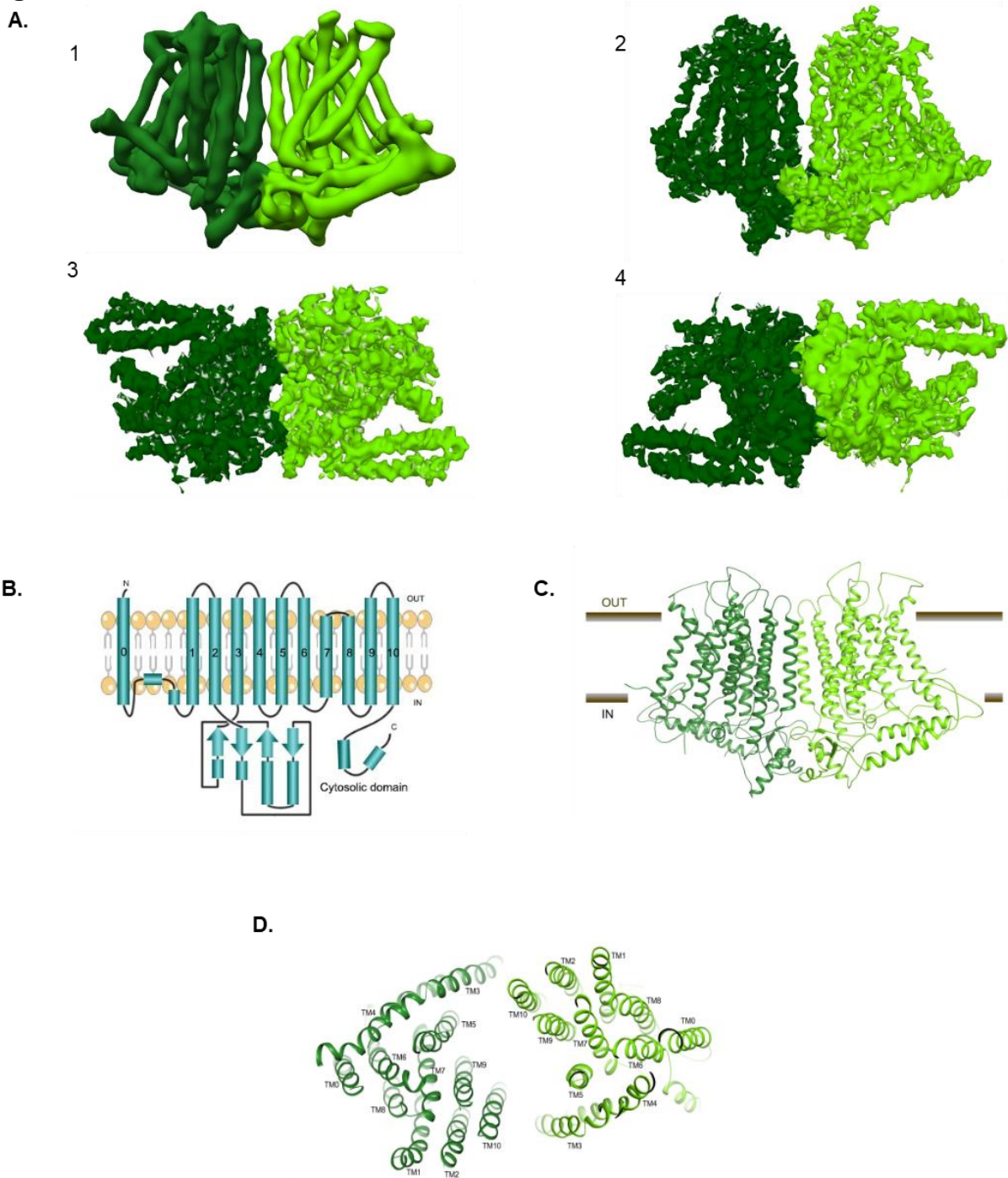
Figure 1. Cryo-EM structure of the OsOSCA1.2 ion channel. (A) From left to right, (1) Parallel to membrane plane view of unsharpened cryoEM density map used for initial chain tracing, (2-4) sharpened 4.9 Å map used for model building and refinement: (2) membrane plane view, (3) extracellular view, and (4) intracellular view. (B) Protein topology of OsOSCA1.2. View of OsOSCA1.2 model from (C) the plane of the cell membrane and (D) from the extracellular side.

16
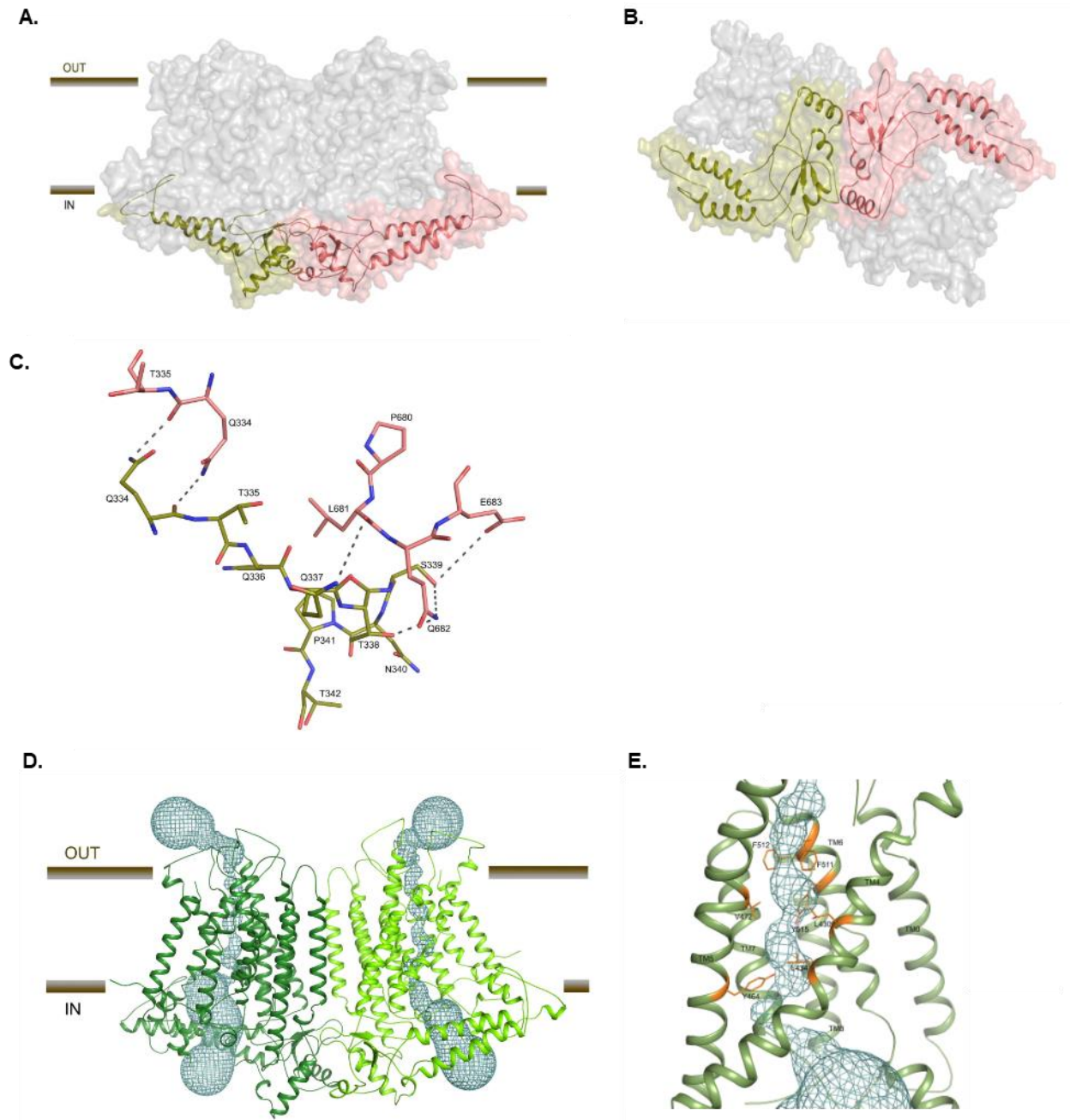
Figure 2

Figure 2. OsOSCA1.2 dimer interface and ion channel pore. (A) OsOSCA1.2 surface representation. The transmembrane domain is shown as gray and the cytoplasmic domain is colored red and yellow. (B) View of OsOSCA1.2 from the cytoplasmic side. (C) Dimer interface residues. (D) Location of the ion conductance pore in both subunits of OsOSCA1.2. The pore pathway is depicted in a cyan mesh. (E) Close-up view of the neck region, showing the residues 'gating' the pore.
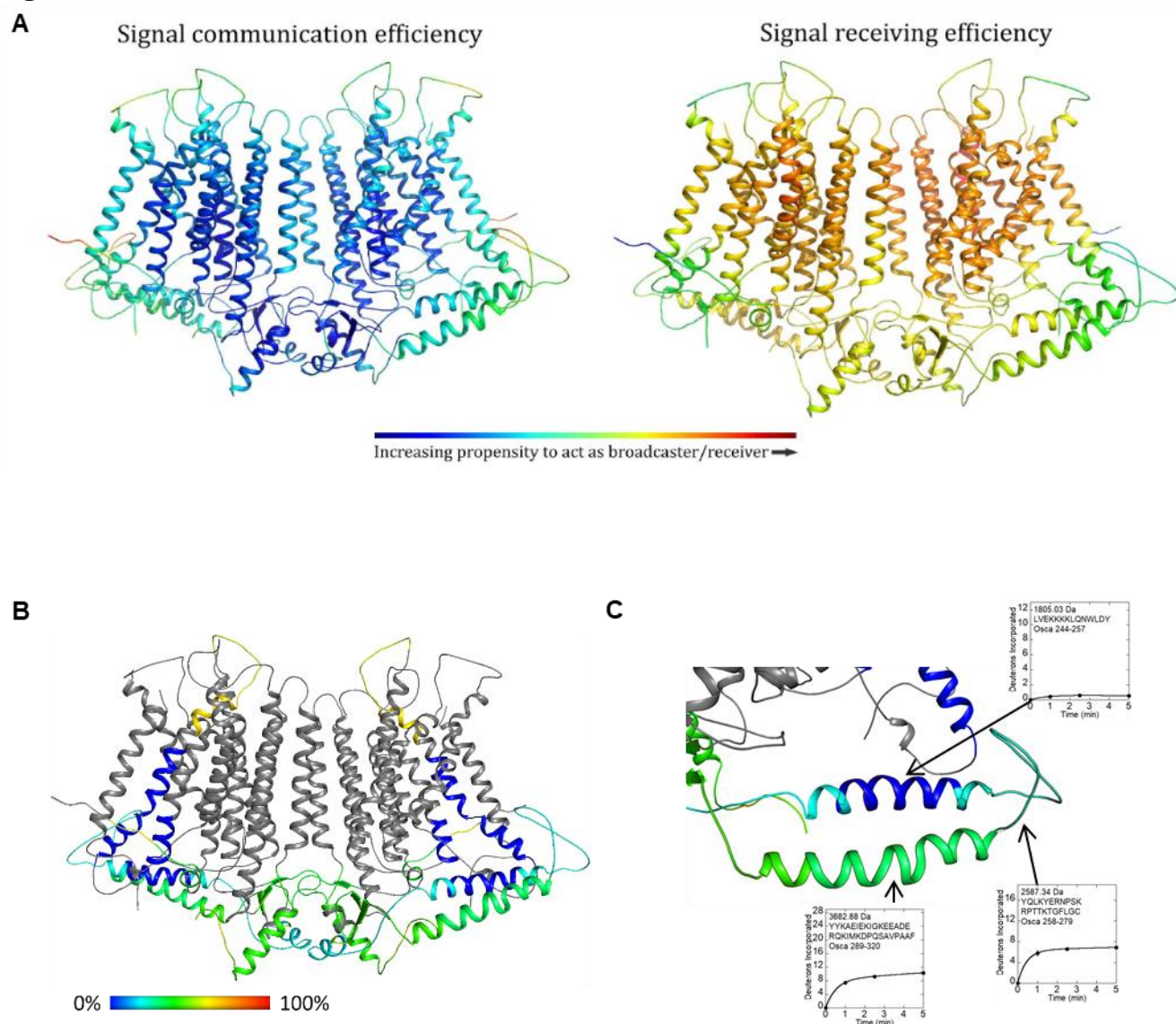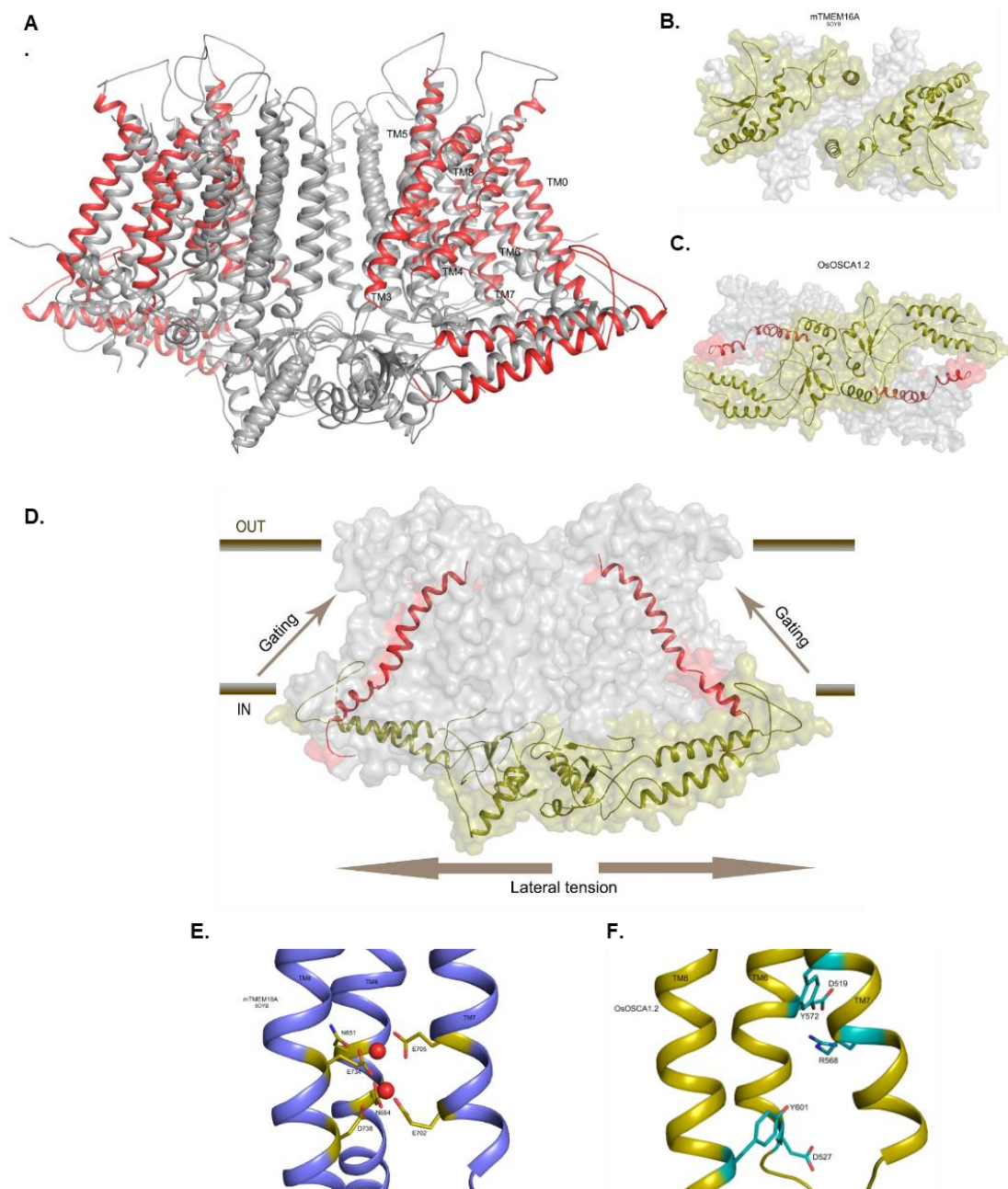
Figure 3

Figure 3. Computational and experimental dynamics of OsOSCA1.2. (A) Results of OsOSCA1.2 embedded in membrane using the Dynomics suite. Panels show a color-coded map superimposed on the model showing signal communication (left) and receiving (right) efficiency. Regions that are colored red are more active while those blue inactive with regards to molecular dynamics prediction. (B) Relative uptake after 5 minutes of exchange. Structure is color scaled and superimposed on model. Regions colored gray yielded no detectable peptide fragments (C) Close-up view of the extended and gating helix. Uptake plots for selected peptides are shown. Corresponding protein segments are outlined.
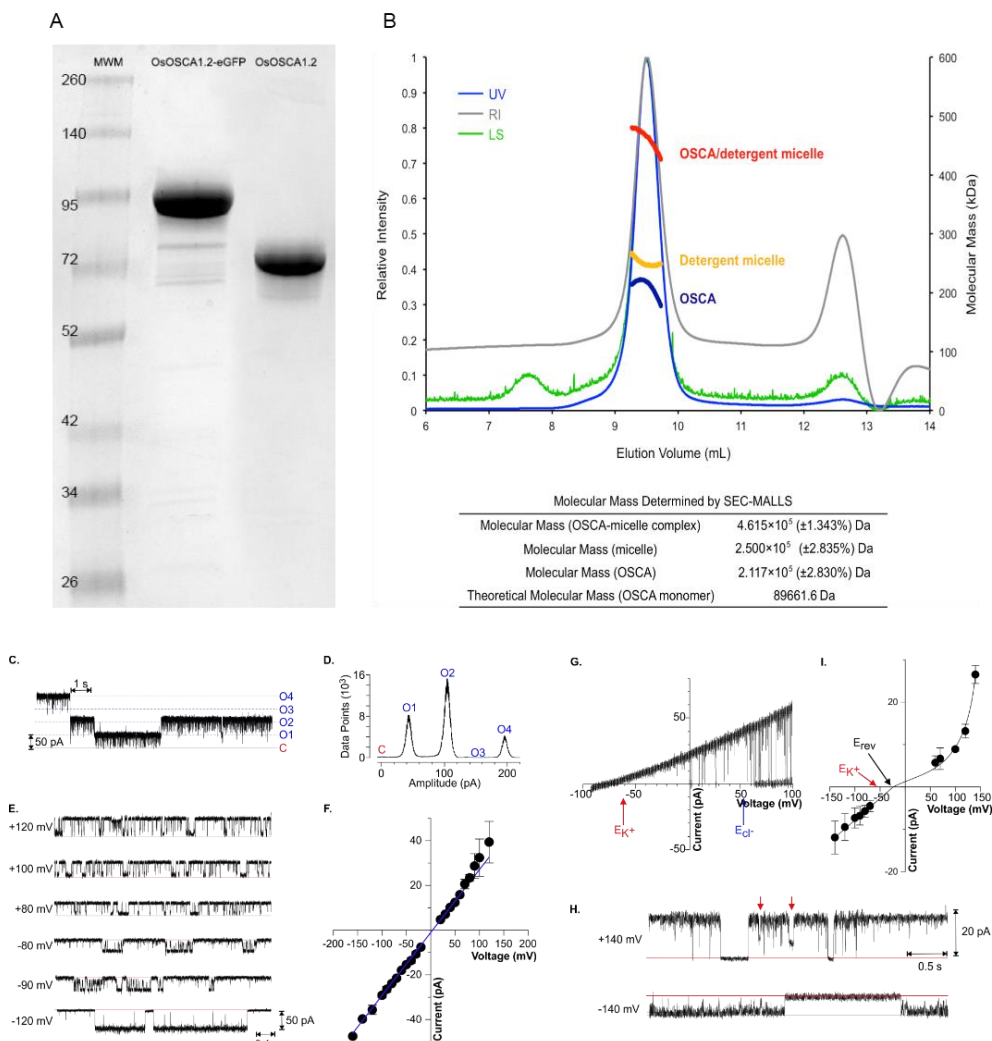
Figure 4

Figure 4. Structural comparisons of OsOSCA1.2 with other TMEM and OSCA structures. (A) Superposition of OsOSCA1.2 and AtOSCA1 (PDB: PYD1). TMs 1, 2, 9, and 10 (shown in gray) close to lipid-filled cleft are nearly superimposable and have little relative movement. Pore-lining helices (TMs 3-7) showed significant movement along with TM0 and TM8 (shown in red). (B) The mTMEM16A soluble domains from intercellular side are separated. (C) OsOSCA1.2 intracellular soluble domains are together and communicate with channel gating helix TM6. (D) General mechanism of OsOSCA1.2 shown in the plane of the lipid membrane. Lateral tension on the inner leaflet side of the lipid bilayer causes a conformational change in the extended helices of the soluble domain, which is coupled to the gating helix TM6 opening pore. (E) Calcium binding site residues of mTMEM16A. Calcium ions are shown as red spheres. (F) The corresponding region of OsOSCA1.2 with charged and polar residues are shown in cyan.

19

Figure S1

Figure S1. Purification and Reconstitution of OsOSCA1.2. (A) SDS-PAGE (sodium dodecyl sulfate polyacrylamide gel electrophoresis) of purified OsOSCA1.2 protein with and without GFP tag. (B) Purified βDDM solubilized OsOSCA1.2 was analysed using size exclusion chromatography in combination with multi-angle laser light scattering (SEC-MALLS). Chromatographs show ultraviolet (UV, blue), refractive index (RI, gray) and light scattering (LS, green) detector readings normalized to the peak maxima (left axis). The thick lines indicate the calculated molecular masses (right axis) of the complete protein/detergent complex (red), as well as the contributions of the detergent (yellow) and protein components (blue) throughout the elution peaks. SEC-MALLS analysis suggests that purified OsOSCA1.2 exists as a dimer in solution. The molecular mass values of the OSCA-micelle complex, the micelle and the protein as determined by SEC-MALLS. The molecular weight of OsOSCA1.2 was calculated from the amino acid sequence. (C-H) Reconstitution of OsOSCA1.2 proteoliposomes into droplet interface bilayers resulted in discrete single channel currents. (C) Example traces of four OsOSCA1.2 channels incorporated into a lipid bilayer recorded in symmetric 150 mM KCl conditions at a holding potential of +140 mV. Upward deflections indicate channel opening representing outward currents (*trans* to *cis*). The zero current (closed state) and conducting (open state) levels are indicated by the red solid and blue dotted lines, respectively. Time and current scales are shown on the top and bottom left corners. (D) Relative histograms illustrating the close and open states distributions for the full-length recordings illustrated on the left. The zero current level (closed state) and conducting (open) state labelled on top correspond to those levels shown on traces on the left. (E) Single channel recordings from a bilayer containing a single active OsOSCA1.2 channel. Recordings were

20

709   obtained in symmetrical conditions (150:150mM KCl) in response to the holding potential
710   indicated on the left of each trace. The zero current levels are indicated by the red solid lines.
711   At positive potentials, upward deflections indicate channel opening representing outward
712   currents (*trans* to *cis*); at negative potentials downward deflections indicate channel opening
713   representing inward currents (*cis* to *trans*). Time and current scales for all traces are shown
714   on the right bottom margin of the last trace. Note the different time scale relative to the traces
715   shown in (C). (F) Single channel current amplitude as a function of voltage obtained from
716   recordings as for those shown in F. In symmetrical 150 mM KCl conditions the channel showed
717   no sign of current rectification, with a unitary conductance of 284 + 2 pS (n=3 bilayers), as
718   determined from a linear regression for values between +120 and – 160 mV. (G) current-
719   voltage ramp (-100 to +100 mV / 1.5 s) of an OsOSCA1.2 channel in asymmetrical 15:150
720   mM KCL (pH 7.4) *cis:trans* conditions. Four consecutive ramps are superimposed. The values
721   for the theoretical Nernst potential for K^+ (E_K+) and Cl^- ($E_{Cl}-$) are indicated by the arrows. (H)
722   Example of single channel recordings from a bilayer containing a single active OsOSCA1.2
723   channel in asymmetrical conditions (15 :150mM KCl) in response to the holding potential
724   indicated on the left of each trace. The zero current levels are indicated by the red solid lines.
725   The red arrows on top of the +140 mV illustrates a brief closure of about 50% the full current
726   amplitude. This 50% state was rarely resolved as long-lasting events as those illustrated by
727   the arrows, but rather appear as a fast flickery behaviour (also see traces in part E). (I) Single
728   channel current amplitude as a function of voltage for OsOSCA1.2 under asymmetrical 15:150
729   mM KCL conditions. The current to voltage relationship was built from steady-state recordings
730   of single-channel activity as those exemplified in part H. The unitary conductance of the inward
731   current and reversal potential (E_{rev}) were determined by fitting of a linear regression of the
732   inward (i.e. negative) currents. E_{rev} (black arrow) was -26 mV and the slope (conductance)
733   103 + 4 pS. The theoretical Nernst potential for K^+ (E_K+) was -54 mV and is indicated by the
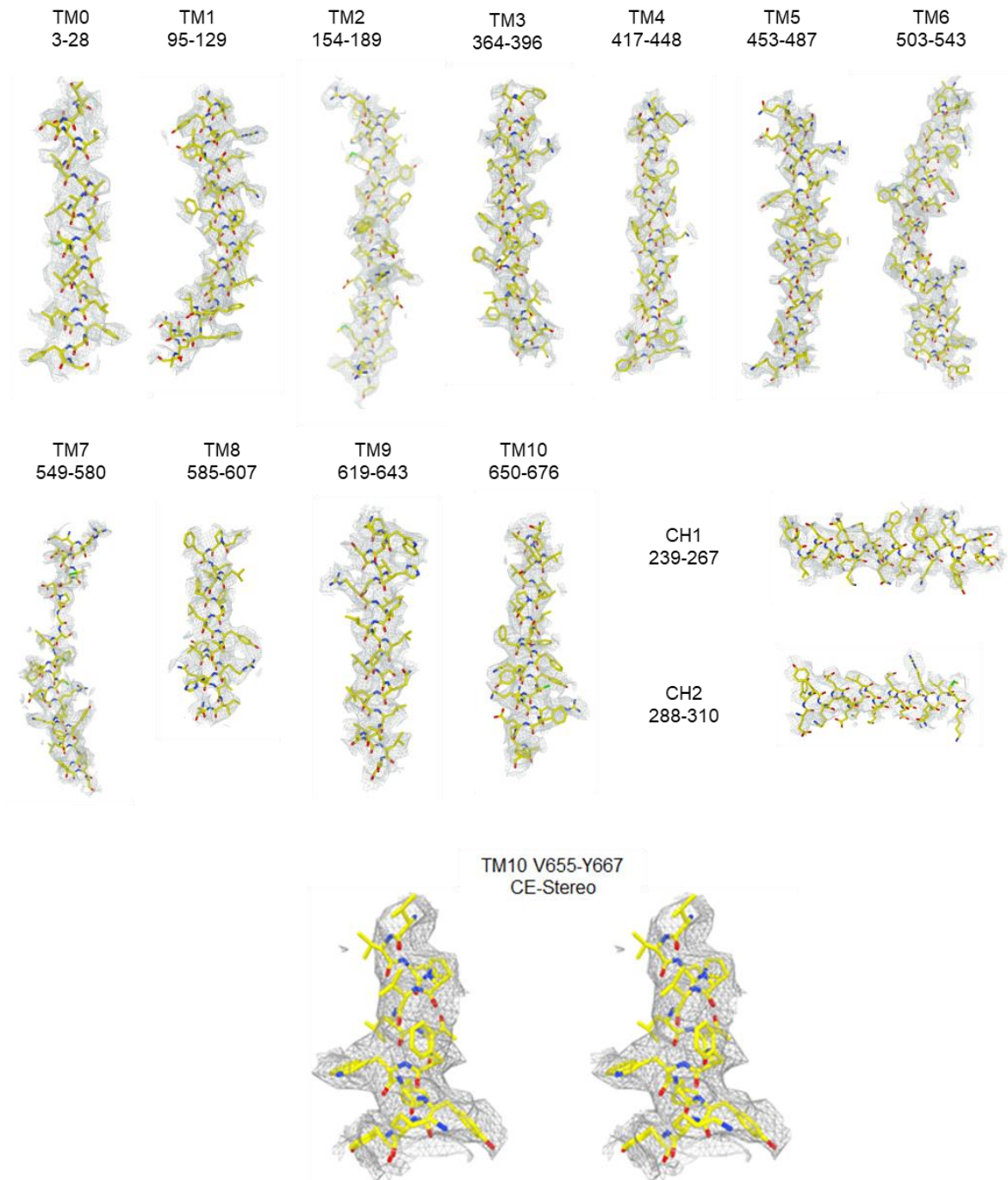734   red arrow.
735
736

737 **Figure S2**
738
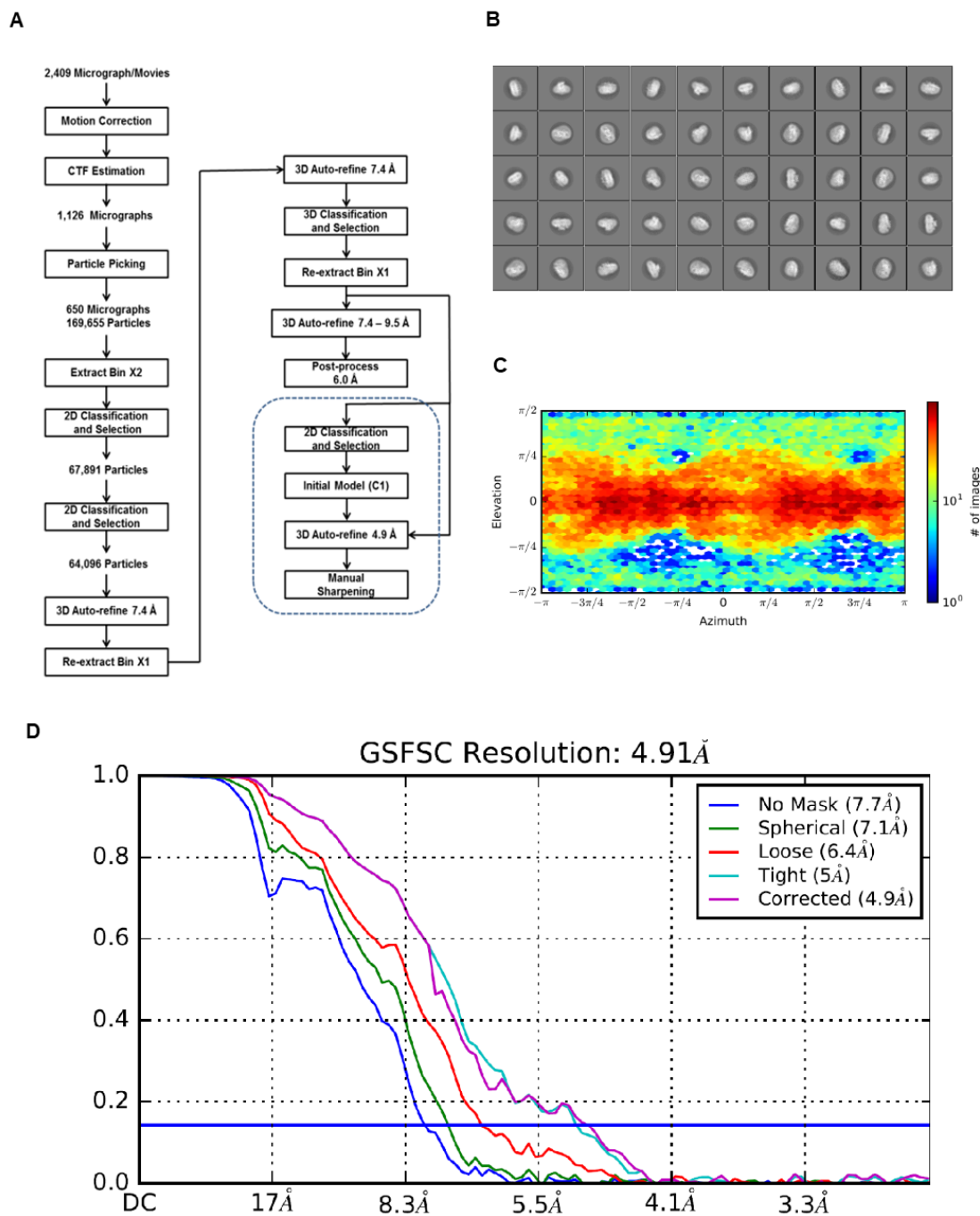
739
740
741
742
743 **Figure S2. Cryo-EM of OscaA1.2.** (A) Data processing flow chart for the 4.9 Å VPP
744 map. (B) 2D-class averages. (C) Angular distribution of particles contributing to the
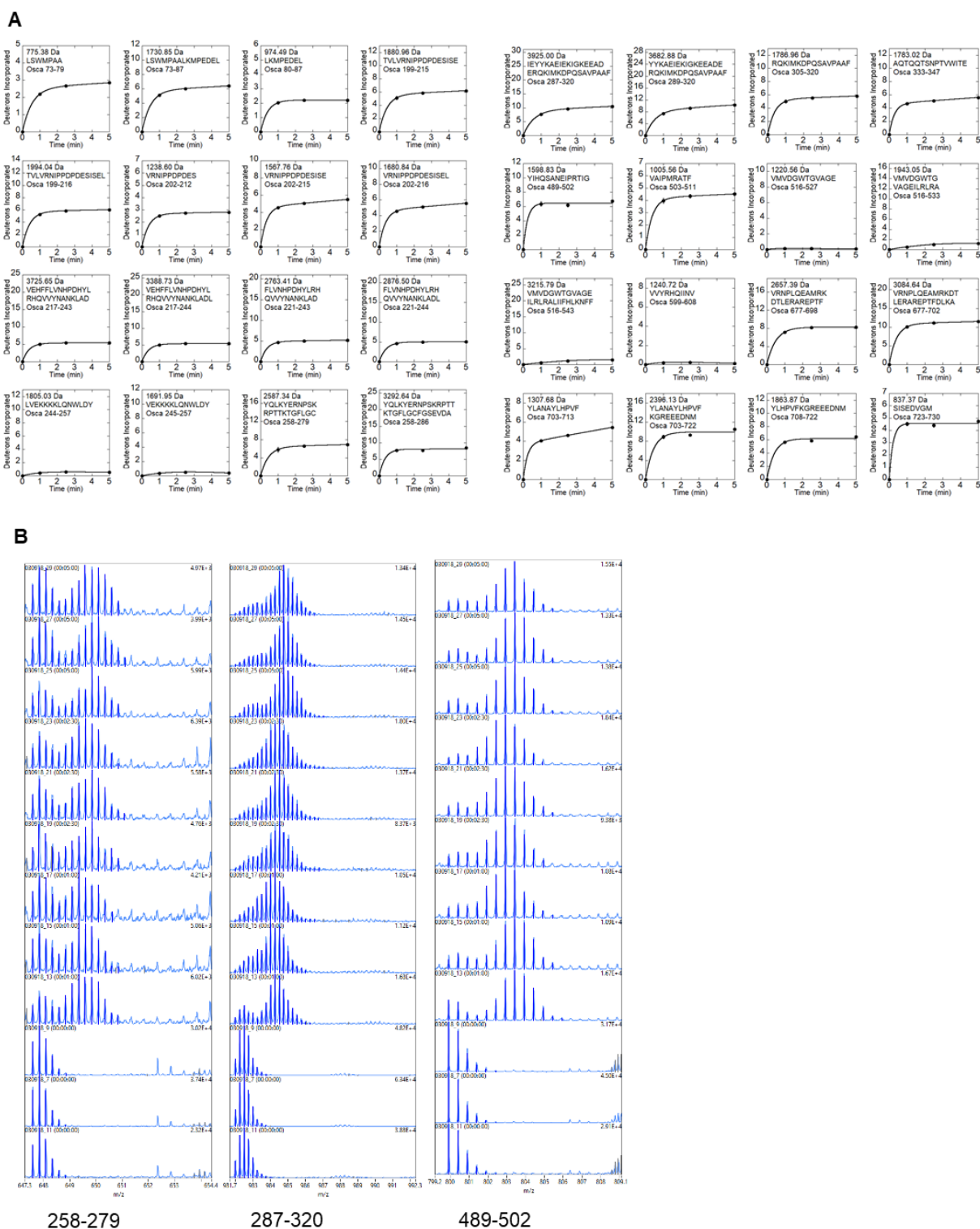745 final 4.9 Å map. (D) GSFSC plots of unmasked and masked maps**.**
746

22

Figure S3

Figure S3. Representative density of OscA1.2. Shown are density maps for all 11 TM helices (TM0-TM10) and the cytoplasmic helices (CH1-CH2) of the soluble domain. A cross-eyed stereo-view of TM10 demonstrating the quality fit of large aromatic sides chins used to sequence registration.
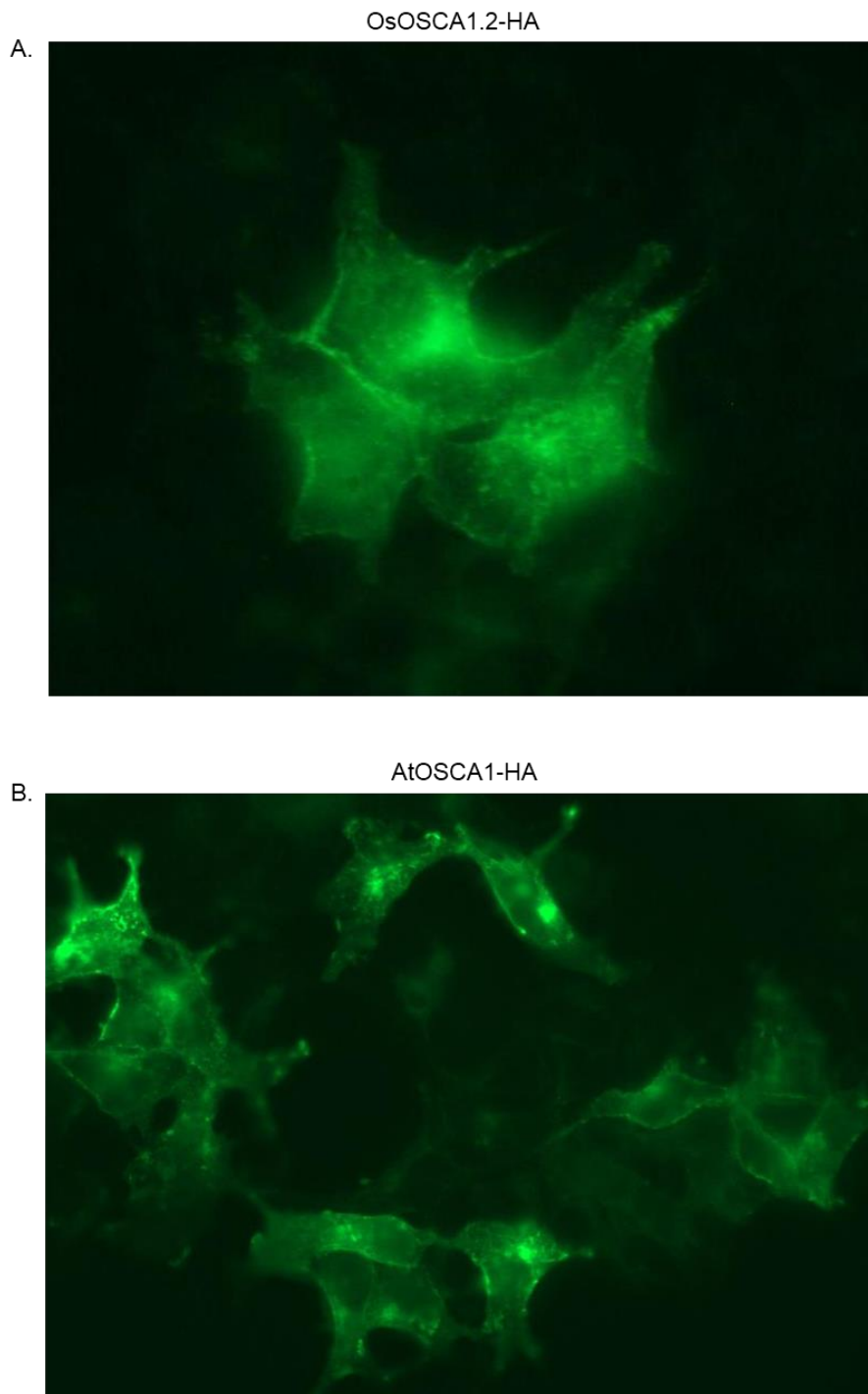
Figure S4

Figure S4. HDXMS Deuterium uptake plots. (A) Deuterium uptake plots for all peptides identified following HDXMS. (B) Representative mass spectra displaying bimodal deuterium uptake.
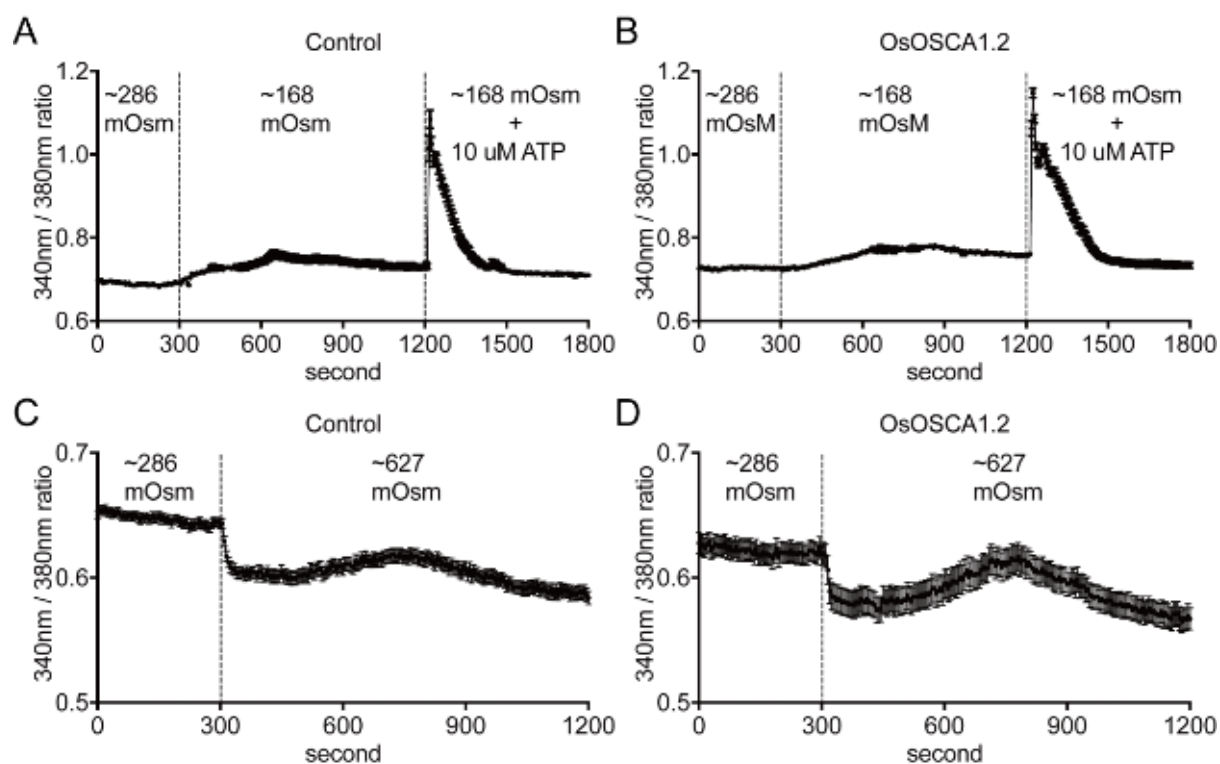
766 **Figure S5**
767

A.

OsOSCA1.2-HA

B.

AtOSCA1-HA

768
769
770
771 **Figure S5. Expression of OsOSCA1.2/AtOSCA1 with C-terminal HA-tag in**
772 **mammalian tsA21 cells.** Immunostain of anti-HA antibody with Alexa 488 suggests
773 exposure of C-terminal HA-tag on the outside of (A) OsOSCA1.2-HA and (B)
774 AtOSCA1-HA. Cells were not permeabilized.
775

Figure S6

Figure S6. OsOSCA1.2 does not alter calcium responses in tsA21 cells under osmotic stresses. Time-resolved intracellular calcium concentration changes were analysed in tsA21 cells transformed with the pCDNA3.1 vector (control) or OsOSCA1.2 as indicated in each panel using a ratiometric fluorescent calcium indicator, Fura-2AM. The ratios of fluorescence intensities in response to excitation at 340 nm and 380 nm were calculated in individual cells and average traces of cells are shown (A and B). tsA21 cells were exposed to hypo-osmotic stress by shifting the osmolality of the bath solution from ~286 mOsm to ~168 mOsm and followed by adding 10 μM ATP. (C and D) tsA21 cells were exposed to hyper-osmotic stress by shifting the osmolarity of the bath solution from ~286 mOsm to ~627 mOsm. Data represent mean ± SE. n = 45 cells in A, 49 cells in B, 39 cells in C, and 23 cells in D.
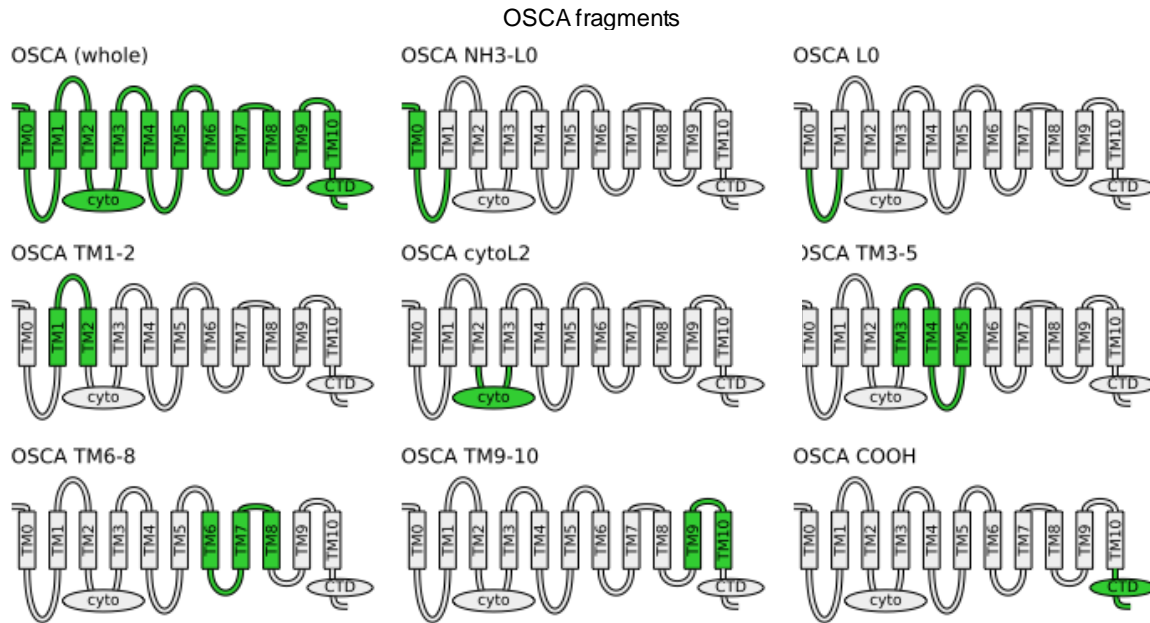
Figure S7


Figure S7. OSCA Fragments Selected for Homolog Searches. OSCA fragments selected for BLAST searches are shown in green while the remainder of the protein is shaded light gray. Due to its extremely short length (23aa), fragment NH3-TM0 was discarded in favor of NH3-L0, which includes loop 0. Two fragments containing L0 (NH3-L0 and L0) were selected to probe for the possible origin of TM0.
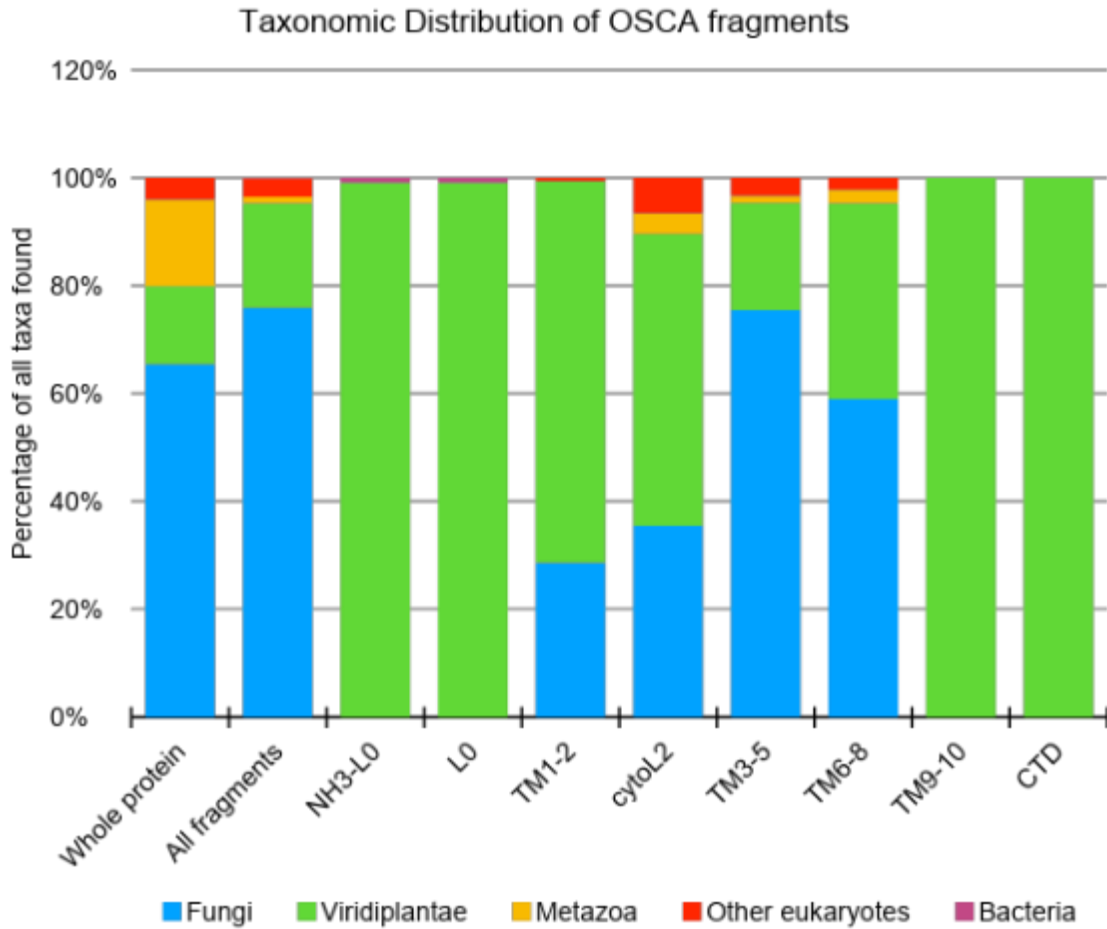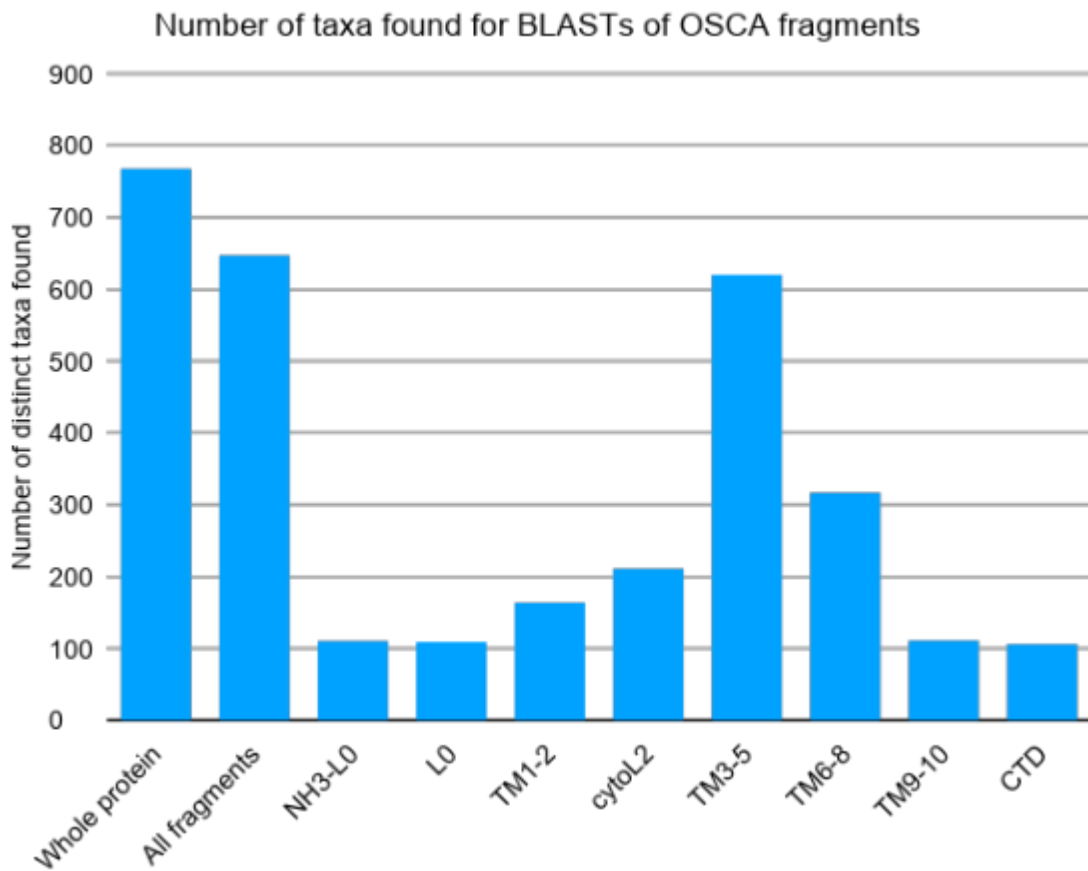
Figure S8

Figure S8. Taxonomic distribution of OSCA fragments. Columns 3 to 10 correspond to different OSCA fragments and show the relative frequency of the taxonomic groups identified in **Table S1**. Plants appear to be the only organisms with sequences similar to TM0, TM9, TM10, Loop 0, and the disordered C-terminal domain.

812 **Figure S9**

813

Number of taxa found for BLASTs of OSCA fragments

814
815

816 **Figure S9. Raw frequency of taxa groups containing the different OSCA**
817 **fragments.** These are the counts used to generate the relative frequencies presented
818 in Table S1 and Figure S9. Note that NH3-L0 and L0 hit the hypothetical enterococcal
819 protein PWS22870 despite matching fewer taxa.

820

29

821 **Table S1**

822

Taxonomic Distribution of selected osOSCA fragments											
		Whole	All fragments	NH3-L0	L0	TM1-2	cytoL2	TM3-5	TM6-8	TM9-10	CTD
BLAST stats											
	Query length	766	N/A	92	69	96	172	118	103	53	94
	Hits	3702	5017	1025	1025	1861	2606	3968	2978	1123	888
Taxonomic stats (%)											
	Eukaryota	100.0%	99.8%	99.1%	99.1%	100.0%	100.0%	100.0%	100.0%	100.0%	100.0%
	Fungi	65.5%	75.9%	0.0%	0.0%	28.7%	35.5%	75.5%	59.0%	0.0%	0.0%
	Viridiplantae	14.5%	19.3%	99.1%	99.1%	70.7%	54.0%	19.8%	36.3%	100.0%	100.0%
	Metazoa	16.0%	1.2%	0.0%	0.0%	0.0%	3.8%	1.3%	2.5%	0.0%	0.0%
	Other eukaryotes	4.0%	3.4%	0.0%	0.0%	0.6%	6.6%	3.4%	2.2%	0.0%	0.0%
	Bacteria	0.0%	0.2%	0.9%	0.9%	0.0%	0.0%	0.0%	0.0%	0.0%	0.0%

823
824
825 **Table S1: Taxonomic distribution of selected OSCA Fragments.** To narrow down
826 the possible regions associated with OSCA's osmo/mechanosensing behavior, the
827 primary sequence of OsOSCA1.2 was split into eight fragments (**Figure S8**). Each
828 fragment was BLASTed against the NCBI's non-redundant protein database (E-value
829 $< 10^{-5}$ and query coverage $\geq 80\%$) and the taxonomic information associated with each
830 hit was extracted. Each column corresponds to a separate fragment. The column
831 labelled "All fragments" consists of the union of taxa after merging all the data.
832 Interestingly, one small hypothetical protein (PWS22870) from *Enterococcus faecium*
833 was found with high significance (E-value $< 10^{-40}$; identity > 70%) and high coverage
834 (88%) for the fragments containing TM0 and L0. However, as PWS22870 does not hit
835 any other bacterial proteins, it cannot be ruled out that this is potentially the result of a
836 sequencing error or a contaminating DNA fragment.
837

References

1. Yuan F, *et al.* (2014) OSCA1 mediates osmotic-stress-evoked Ca2+ increases vital for osmosensing in Arabidopsis. *Nature* 514(7522):367-371.

2. Knight H, Trewavas AJ, & Knight MR (1997) Calcium signalling in Arabidopsis thaliana responding to drought and salinity. *Plant J* 12(5):1067-1078.

3. Stephan AB, Kunz HH, Yang E, & Schroeder JI (2016) Rapid hyperosmotic-induced Ca2+ responses in Arabidopsis thaliana exhibit sensory potentiation and involvement of plastidial KEA transporters. *Proc Natl Acad Sci U S A* 113(35):E5242-5249.

4. Murthy SE, *et al.* (2018) OSCA/TMEM63 are an Evolutionarily Conserved Family of Mechanically Activated Ion Channels. *Elife* 7.

5. Medrano-Soto A, *et al.* (2018) Bioinformatic characterization of the Anoctamin Superfamily of Ca2+-activated ion channels and lipid scramblases. *PLoS One* 13(3):e0192851.

6. Jojoa-Cruz S, *et al.* (2018) Cryo-EM structure of the mechanically activated ion channel OSCA1.2. *Elife* 7.

7. Zhang M, *et al.* (2018) Structure of the mechanosensitive OSCA channels. *Nat Struct Mol Biol* 25(9):850-858.

8. Barad BA, *et al.* (2015) EMRinger: side chain-directed model and map validation for 3D cryo-electron microscopy. *Nature methods* 12(10):943-946.

9. Saier MH, Jr., *et al.* (2016) The Transporter Classification Database (TCDB): recent advances. *Nucleic acids research* 44(D1):D372-379.

10. Brunner JD, Lim NK, Schenck S, Duerst A, & Dutzler R (2014) X-ray structure of a calcium-activated TMEM16 lipid scramblase. *Nature* 516(7530):207-212.

11. Dang S, *et al.* (2017) Cryo-EM structures of the TMEM16A calcium-activated chloride channel. *Nature* 552(7685):426-429.

12. Rai A, Suprasanna P, D'Souza SF, & Kumar V (2012) Membrane topology and predicted RNA-binding function of the 'early responsive to dehydration (ERD4)' plant protein. *PLoS One* 7(3):e32658.

13. Krissinel E & Henrick K (2007) Inference of macromolecular assemblies from crystalline state. *J Mol Biol* 372(3):774-797.

14. Liu X, Wang J, & Sun L (2018) Structure of the hyperosmolality-gated calcium-permeable channel OSCA1.2. *Nat Commun* 9(1):5060.

15. Smart OS, Breed J, Smith GR, & Sansom MS (1997) A novel method for structure-based prediction of ion channel conductance properties. *Biophys J* 72(3):1109-1126.

16. Li H, Chang YY, Lee JY, Bahar I, & Yang LW (2017) DynOmics: dynamics of structural proteome and beyond. *Nucleic acids research* 45(W1):W374-W380.

17. Wales TE & Engen JR (2006) Hydrogen exchange mass spectrometry for the study of proteins. *Mass Spec. Rev.* 25:158-170.

18. Truhlar SME, Croy CH, Torpey JW, Koeppe JR, & Komives EA (2006) Solvent Accessibility of Protein Surfaces by Amide H/2H Exchange MALDI-TOF Mass Spectrometry. *J. Am. Soc. Mass Spectrom.* 17:1490-1497.

19. Hou C, *et al.* (2014) DUF221 proteins are a family of osmosensitive calcium-permeable cation channels conserved across eukaryotes. *Cell research* 24(5):632-635.

885 20. Paulino C, Kalienkova V, Lam AKM, Neldner Y, & Dutzler R (2017) Activation
886   mechanism of the calcium-activated chloride channel TMEM16A revealed by
887   cryo-EM. *Nature* 552(7685):421-425.
888 21. Li MJ, Guttman M, & Atkins WM (2018) Conformational dynamics of P-
889   glycoprotein in lipid nanodiscs and detergent micelles reveal complex motions
890   on a wide time scale. *J. Biol. chem.*:6297-6307.
891 22. Slotboom DJ, Duurkens RH, Olieman K, & Erkens GB (2008) Static light scattering
892   to characterize membrane proteins in detergent solution. *Methods* 46(2):73-82.
893 23. Mulligan C*, et al.* (2009) The substrate-binding protein imposes directionality on
894   an electrochemical sodium gradient-driven TRAP transporter. *Proc Natl Acad Sci*
895   *U S A* 106(6):1778-1783.
896 24. Hwang WL, Chen M, Cronin B, Holden MA, & Bayley H (2008) Asymmetric
897   droplet interface bilayers. *J Am Chem Soc* 130(18):5878-5879.
898 25. Leptihn S*, et al.* (2013) Constructing droplet interface bilayers from the contact
899   of aqueous droplets in oil. *Nat Protoc* 8(6):1048-1057.
900 26. Syeda R, Holden MA, Hwang WL, & Bayley H (2008) Screening blockers against a
901   potassium channel with a droplet interface bilayer array. *J Am Chem Soc*
902   130(46):15543-15548.
903 27. Coste B*, et al.* (2012) Piezo proteins are pore-forming subunits of mechanically
904   activated channels. *Nature* 483(7388):176-181.
905 28. Shaff J, Schultz B, Craft EJ, Clark RT, & Kochian LV (2010) GEOCHEM-EZ: a
906   chemical speciation program with greater power and flexibility. *Plant and Soil*
907   *Journal* 330:207-214.
908 29. Adams PD*, et al.* (2010) PHENIX: a comprehensive Python-based system for
909   macromolecular structure solution. *Acta Crystallogr D Biol Crystallogr* 66(Pt
910   2):213-221.
911 30. Emsley P, Lohkamp B, Scott WG, & Cowtan K (2010) Features and development
912   of Coot. *Acta Crystallogr D Biol Crystallogr* 66(Pt 4):486-501.
913 31. Chen Q*, et al.* (2017) Structure of mammalian endolysosomal TRPML1 channel in
914   nanodiscs. *Nature* 550(7676):415-418.
915 32. Zhang K (2016) Gctf: Real-time CTF determination and correction. *J Struct Biol*
916   193(1):1-12.
917 33. Scheres SH (2012) A Bayesian view on cryo-EM structure determination. *J Mol*
918   *Biol* 415(2):406-418.
919 34. Punjani A, Rubinstein JL, Fleet DJ, & Brubaker MA (2017) cryoSPARC: algorithms
920   for rapid unsupervised cryo-EM structure determination. *Nature methods*
921   14(3):290-296.
922 35. Kucukelbir A, Sigworth FJ, & Tagare HD (2014) Quantifying the local resolution
923   of cryo-EM density maps. *Nature methods* 11(1):63-65.
924 36. Grynkiewicz G, Poenie M, & Tsien RY (1985) A new generation of Ca2+ indicators
925   with greatly improved fluorescence properties. *The Journal of biological*
926   *chemistry* 260(6):3440-3450.
927 37. Schindelin J*, et al.* (2012) Fiji: an open-source platform for biological-image
928   analysis. *Nature methods* 9(7):676-682.
929